

# Myeloid cell-specific topoisomerase 1 inhibition using DNA origami mitigates neuroinflammation

Keying Zhu<sup>1,\*</sup> , Yang Wang<sup>2,†</sup> , Heela Sarlus<sup>1,†</sup> , Keyi Geng<sup>3,†</sup> , Erik Nutma<sup>4</sup>, Jingxian Sun<sup>5,6,7</sup>, Shin-Yu Kung<sup>1</sup> , Cindy Bay<sup>1</sup> , Jinming Han<sup>1</sup> , Jin-Hong Min<sup>1</sup>, Irene Benito-Cuesta<sup>1</sup>, Harald Lund<sup>8</sup> , Sandra Amor<sup>4</sup> , Jun Wang<sup>5,6,7</sup> , Xing-Mei Zhang<sup>1</sup> , Claudia Kutter<sup>3</sup> , André Ortlieb Guerreiro-Cacais<sup>1</sup> , Björn Högberg<sup>2</sup>  & Robert A Harris<sup>1,\*\*</sup> 

## Abstract

Targeting myeloid cells, especially microglia, for the treatment of neuroinflammatory diseases such as multiple sclerosis (MS), is underappreciated. Our *in silico* drug screening reveals topoisomerase 1 (TOP1) inhibitors as promising drug candidates for microglial modulation. We show that TOP1 is highly expressed in neuroinflammatory conditions, and TOP1 inhibition using camptothecin (CPT) and its FDA-approved analog topotecan (TPT) reduces inflammatory responses in microglia/macrophages and ameliorates neuroinflammation *in vivo*. Transcriptomic analyses of sorted microglia from LPS-challenged mice reveal an altered transcriptional phenotype following TPT treatment. To target myeloid cells, we design a nanosystem using  $\beta$ -glucan-coated DNA origami (MyloGami) loaded with TPT (TopoGami). MyloGami shows enhanced specificity to myeloid cells while preventing the degradation of the DNA origami scaffold. Myeloid-specific TOP1 inhibition using TopoGami significantly suppresses the inflammatory response in microglia and mitigates MS-like disease progression. Our findings suggest that TOP1 inhibition in myeloid cells represents a therapeutic strategy for neuroinflammatory diseases and that the myeloid-specific nanosystems we designed may also benefit the treatment of other diseases with dysfunctional myeloid cells.

**Keywords** DNA nanostructure; inflammation; macrophage; microglia; topoisomerase

**Subject Categories** Immunology; Neuroscience; Pharmacology & Drug Discovery

DOI 10.15252/embr.202154499 | Received 12 December 2021 | Revised 1 May 2022 | Accepted 4 May 2022 | Published online 20 May 2022

EMBO Reports (2022) 23: e54499

## Introduction

The functions of the innate immune system are predominantly executed by cells of the myeloid lineage (“myeloid cells”), which comprise monocytes, dendritic cells, macrophages, and microglia. Myeloid cells play important roles in the regulation of inflammation, non-specific host defense against microbes, the clearance of tissue debris, and the remodeling of tissues.

Neuroinflammation refers to inflammatory responses occurring within the central nervous system (CNS) and is a common feature of various disease states or etiology that may be acute or chronic. Emerging evidence has indicated a pivotal role of myeloid cells in the immunopathology of CNS neuroinflammatory conditions such as multiple sclerosis (MS), amyotrophic lateral sclerosis (ALS), and rodent experimental autoimmune encephalomyelitis (EAE). Infiltrating monocyte-derived macrophages destroy neurons and oligodendrocytes during MS, and the action of pro-inflammatory microglia/macrophages drives motor neuron death in ALS. A recent human genome-wide association study including 47,429 MS patients and 68,374 control cases determined that MS susceptibility genes were enriched in microglia (International Multiple Sclerosis Genetics Consortium, 2019). The *C9orf72* gene, whose dysregulation accounts for the most frequent genetic cause of familial ALS, is highly expressed in myeloid cells (O’Rourke *et al*, 2016). The absence of *C9orf72* in

1 Applied Immunology and Immunotherapy, Department of Clinical Neuroscience, Karolinska Institutet, Center for Molecular Medicine, Karolinska University Hospital, Stockholm, Sweden

2 Department of Medical Biochemistry and Biophysics, Karolinska Institutet, Stockholm, Sweden

3 Department of Microbiology, Tumor and Cell Biology, Science for Life Laboratory, Karolinska Institute, Stockholm, Sweden

4 Department of Pathology, Amsterdam UMC, Amsterdam, The Netherlands

5 Department of Integrative Medicine and Neurobiology, School of Basic Medical Sciences, Shanghai, China

6 State Key Laboratory of Medical Neurobiology and MOE Frontiers Center for Brain Science, Shanghai, China

7 Shanghai Medical College, Fudan University, Shanghai, China

8 Department of Physiology and Pharmacology, Karolinska Institutet, Center for Molecular Medicine, Karolinska University Hospital, Stockholm, Sweden

\*Corresponding author. Tel: +46 760706722; E-mail: keying.zhu@ki.se

\*\*Corresponding author. Tel: +46 (0) 8 517 765 61; E-mail: robert.harris@ki.se

†These authors contributed equally to this work

myeloid cells disturbs homeostasis and predisposes individuals to neuroinflammatory disorders (McCauley *et al.*, 2020).

However, very few medications to specifically target myeloid cells have been developed to date. In this study, we designed a drug-screening strategy using *Connectivity Map* (CMAP) to identify drugs with the potential to modulate the microglial function and repurposed the FDA-approved topoisomerase 1 (TOP1) inhibitor topotecan (TPT) as an effective therapeutic to regulate inflammatory responses in microglia and neuroinflammation. TOP1 disentangles supercoiled DNA during transcription by nicking one single strand, allowing it to rotate around the other intact DNA single strand, followed by re-ligation. TOP1 activities are required for all genes to resolve topological torsion during transcription, DNA replication, and chromatin remodeling. However, TOP1 activities at the promoters of housekeeping genes could be redundant, whereas for genes whose transcription require more transcriptional elongation, histone modifications and nucleosome remodeling, such as inducible inflammatory genes, sufficient TOP1 activity is indispensable (Smale & Natoli, 2014; Rialdi *et al.*, 2016; Marazzi *et al.*, 2018). TOP1 inhibitors may thus limit the transcription of inducible genes with few effects on housekeeping genes.

Whether TOP1 is involved in microglial activation and neuroinflammatory conditions, such as multiple sclerosis, has not been examined before. Herein, we report an increased TOP1 expression in both activated microglia *in vitro* and during neuroinflammatory disease states, including MS brain pathology, indicating TOP1 a viable treatment target. To achieve a more controllable and specific delivery of TPT to myeloid cells and to understand whether specifically inhibiting TOP1 activity in myeloid cells is sufficient to combat neuroinflammation, we designed a novel tool to target myeloid cells using DNA origami (herein referred to as MyloGami) and developed a myeloid cell-specific TOP1 inhibitor (TopoGami) by loading TPT into MyloGami. We demonstrate that MyloGami had a high affinity to myeloid cells and that TopoGami significantly improved MS-like diseases in a similar fashion to TPT, further highlighting the importance of innate immune regulation in the context of EAE/MS.

Our findings lead us to propose TOP1 as a treatment target for neuroinflammation, and that the FDA-approved drug topotecan could be repurposed and translated for treating neuroinflammatory disorders. In addition, the MyloGami we designed will be of great value for future drug development or studies that demand the specific targeting of myeloid cells.

## Results

### Identification of TOP1 inhibitors as potent microglial modulators

To find suitable compounds that alter microglia states, we used a repurposing approach by utilizing a *Connectivity Map* (CMAP) discovery strategy (Lamb *et al.*, 2006), thus enabling a relatively quicker translation of an existing approved drug to a new clinical application. We analyzed a dataset that contains transcriptomic data from human microglia stimulated with defined stimulants to induce different phenotypes: M1(LPS/IFN $\gamma$ ), M2a (IL-4/IL-13), M2c (-4/IL-13/IL-10), and Mtgfb (TGF- $\beta$ ) (Fig 1A). Although the nomenclature of M1/M2 microglial activation is now considered to be an oversimplified dogma overlooking the heterogeneity and complexity of microglial

activation states, *in vitro* stimulation of microglia with defined stimuli clearly distinguishes the pro-inflammatory M1 phenotype from immunoregulatory M2-subphenotypes (M2a/M2c/Mtgfb). We will use the terminology as it relates to that used in the dataset.

The six differential gene expression patterns from resting microglia (M0) to M2a/M2c/Mtgfb and M1 to M2a/M2c/Mtgfb activation states were determined. Four compounds (camptothecin, alsterpaullone, GW-8510, and H-7) were identified in the positively correlated drug list in each of these six patterns, indicating they might reprogram microglia into an immunoregulatory phenotype (Fig 1B). Compared with the other three identified compounds, camptothecin (CPT) had an overall high CMAP score among all the six patterns (Fig 1C), and its mechanism of action as a topoisomerase 1 (TOP1) inhibitor is well understood. In addition, derivatives of CPT such as topotecan and irinotecan have been FDA approved for clinical use. We have also listed other potential compounds and drugs from the CMAP screening that might skew microglia towards an immunoregulatory phenotype (Table EV1). Therefore, we decided to evaluate the possibility of repurposing TOP1 inhibitors to modulate neuroinflammation.

### TOP1 expression is elevated in neuroinflammatory conditions

We first addressed whether TOP1 levels were altered during neuroinflammatory conditions as TOP1 is the only known cellular target of CPT (Pommier, 2006). We cultured primary microglia from adult mice and stimulated them with LPS/IFN $\gamma$  (Fig 2A). We observed an increased *Top1* mRNA expression after 2-h stimulation, which gradually subsided overtime (Fig 2B). The intracellular/intranuclear regulation of TOP1 activity is not fully elucidated, but some proteins have been proposed to regulate the recruitment of TOP1 to chromatin or TOP1 degradation. Among these, BTB/POZ domain-containing protein 1 (BTBD1) is known to specifically bind to TOP1 and may function as a TOP1 degradation regulator (Husain *et al.*, 2016); the DNA end-processing enzyme TDP1 counteracts the biological function of TOP1 cleavage complexes (Zaksauskaite *et al.*, 2021); the serine/arginine-rich splicing factor 1 (SRSF1) inhibits the recruitment of TOP1 from the nucleoplasm to the nucleolus (Girstun *et al.*, 2019). We observed a concomitant decrease in the mRNA expression of these three negative regulators of TOP1 following microglial activation (Fig 2C). We further confirmed an increased expression of TOP1 protein in microglia following LPS/IFN $\gamma$  stimulation by Western blotting and immunostaining (Fig 2D–F and H), indicating an active involvement of TOP1 during microglial activation.

We also evaluated TOP1 expression in animal models with neuroinflammatory manifestation. We first employed the experimental autoimmune encephalomyelitis (EAE) model for investigation. EAE features activated Th1/Th17 cell infiltration into the CNS together with pro-inflammatory myeloid cells, causing devastating demyelination reflected by clinical motor symptoms (Constantinescu *et al.*, 2011). Thus, EAE mimics the immunopathogenesis of MS to a large extent. We observed an increased TOP1 expression in the spinal cords obtained from mice at the EAE peak stage (score 3), as evidenced by both immunofluorescent staining (Fig 2G, I and J) and Western blotting (Fig 2K and L). TOP1 is a nuclear protein, and accordingly, the enhanced TOP1 immunoreactivity was mainly evident in the nuclear compartment of F4/80-expressing myeloid cells, which represent the infiltrating monocytes/macrophages in the context of EAE (Fig 2G and I). We next employed the LPS challenge

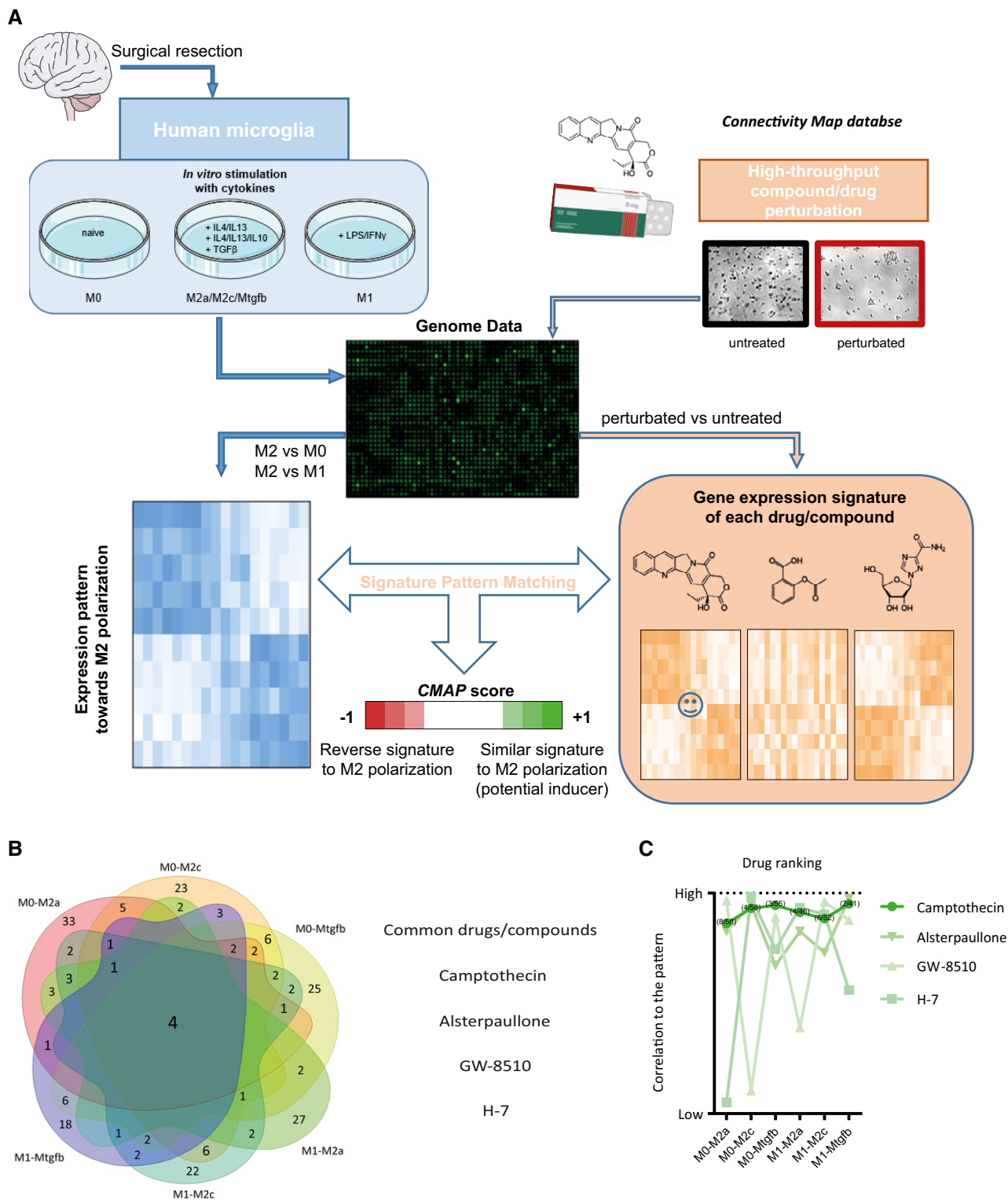


**Figure 1. Connectivity Map-based drug screening and repurposing.**

- A A schematic overview of the screening process. A dataset containing human microglia stimulated with indicated cytokines to induce different phenotypes was analyzed (Healy *et al*, 2016a; Data ref: Healy *et al*, 2016b). The differential gene expression profiles from patterns M0 to M2a/M2c/Mtgfb and M1 to M2a/M2c/Mtgfb were identified respectively using the NCBI GEO2R tool. Top 1,000 differential genes were selected, and the up-regulated genes and the down-regulated genes were converted to identifiers based on the Affymetrix HG-U133A chip, followed by analysis and matching with Connectivity Map.
- B Four overlapping compounds/drugs were identified in each of the 6 patterns: camptothecin, alsterpaullone, GW-8510, and H-7.
- C Compared with the other candidates, camptothecin has the highest overall correlation to inducing all these 6 patterns.

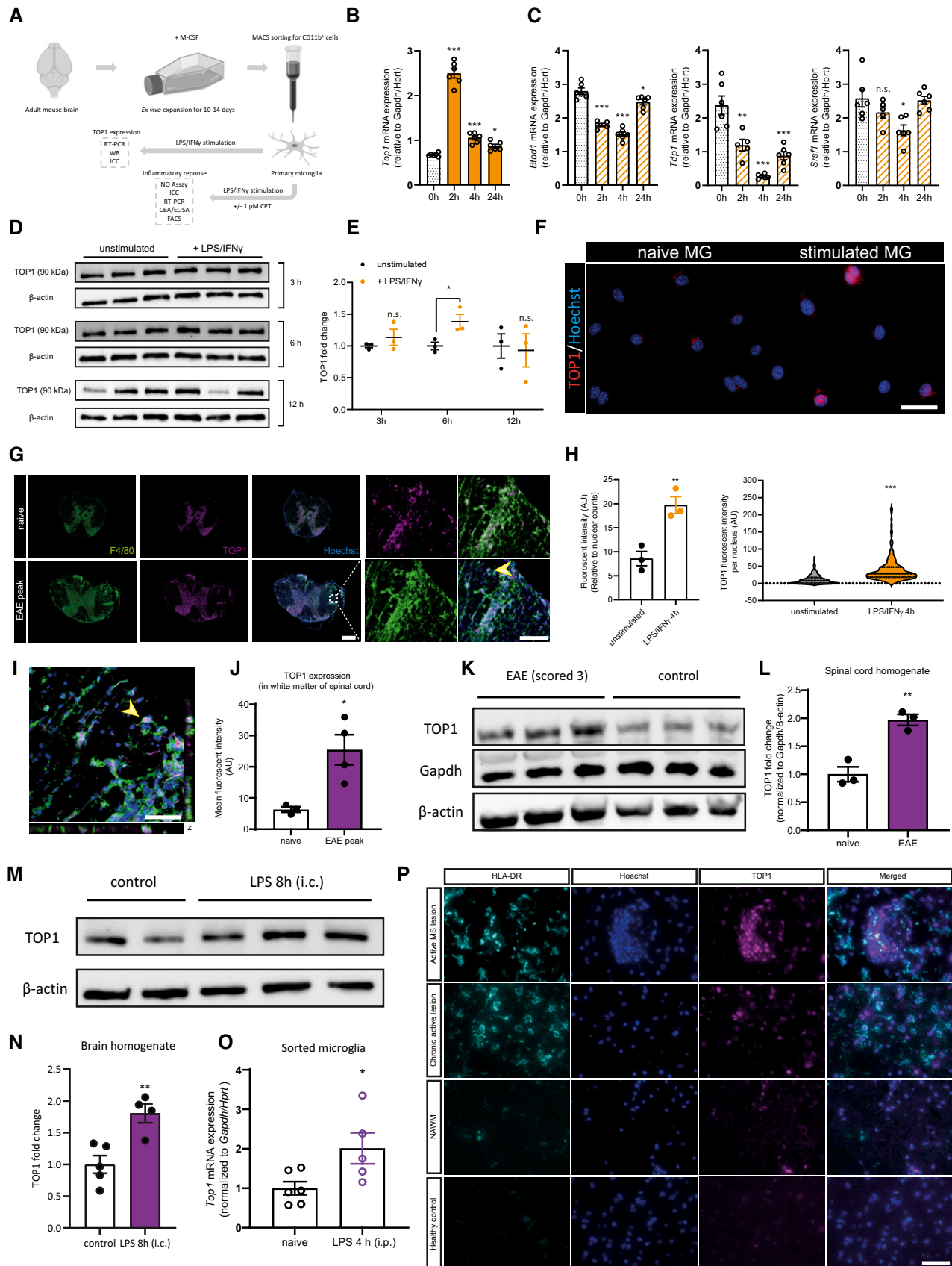


Figure 2.

**Figure 2. TOP1 expression is increased in neuroinflammatory conditions.**

- A A schematic overview of the *in vitro* experiments.
- B, C Kinetic change of mRNA expression of *Top1*, *Btbd1*, *Tdp1*, and *Srsf1* in microglia following LPS/IFN $\gamma$  stimulation ( $n = 6$ , technical replicates).
- D, E The protein expression of TOP1 was detected by Western blotting ( $n = 3$ , biological replicates).
- F–H Immunostaining of TOP1 (red) in stimulated microglia (4 h after LPS/IFN $\gamma$  stimulation) or resting microglia, co-stained with Hoechst (blue) (bar = 20  $\mu\text{m}$ ); for the lower-left panel (H),  $n = 3$  technical replicates per group (2–5 random fields per well were analyzed); for the lower right panel, 201 cells from unstimulated microglia and 256 cells from stimulated microglia were analyzed.
- G Immunofluorescent staining of spinal cord sections from mice at EAE peak and control mice with anti-F4/80 (green), TOP1 (magenta), and nuclei with Hoechst (blue). For the left panels, bar = 400  $\mu\text{m}$ ; for the magnified panels, bar = 100  $\mu\text{m}$ . The yellow arrowhead indicates a representative F4/80 $^{+}$  cell with high TOP1 expression.
- I A magnified image of the selected region (white box) in (G); bar = 50  $\mu\text{m}$ ; the yellow arrowhead indicates the representative F4/80 $^{+}$  cell with increased TOP1 expression in the nucleus in (G).
- J The mean fluorescent intensity of TOP1 expression in the white matter in (G) was graphed;  $n = 3$ –4 mice per group with 3–5 sections from each mouse.
- K TOP1 expression in the spinal cord homogenates of EAE mice dissected at disease peak (scored 3) or control mice were examined by Western blotting.
- L The quantification of TOP1 protein expression of Western blot bands in (K) with normalization to GAPDH and  $\beta$ -actin ( $n = 3$  biological samples).
- M, N Western blotting of TOP1 expression from brain homogenates of mice receiving intracisternal LPS injection or PBS after 8 h ( $n = 4$  or 5 biological samples).
- O Microglia were sorted from LPS challenged mice (i.p) after 4 h or naive mice, and the mRNA expression of TOP1 was graphed ( $n = 5$  or 6 biological samples).
- P Brain sections from healthy control and MS brain tissues, including the active MS lesion, chronic active lesion, and the normal-appearing white matter (NAWM), were stained with anti-HLA-DR, anti-TOP1, and co-stained with Hoechst (bar = 50  $\mu\text{m}$ ).

Data information: Data are presented as the mean  $\pm$  SEM. \* $P < 0.05$ ; \*\* $P < 0.01$ ; \*\*\* $P < 0.001$ ; n.s. = no statistical significance. Statistical analyses were performed using two-way ANOVA with Dunnett's Multiple Comparison test for (B and C), and the rest were performed using the student's unpaired two-tailed  $t$ -test.

Source data are available online for this figure.

model, as myeloid cells are the main effector cells in this model, and it stimulates a robust innate immune response characterized by the activation of myeloid cells. It has been reported that one systemic LPS challenge induces robust microglial activation, depressive sickness behavior, and persistent neuroinflammation, even when peripheral immune activation is tempered (Qin *et al*, 2007). In mouse microglia sorted 4 h post-LPS challenge (i.p), we observed an upregulation of *Top1* mRNA expression (Fig 2O). In parallel, when 10 ng LPS was delivered directly into the CNS via intracisternal injection, we also observed an increased TOP1 protein expression in the brains 8 h later (Fig 2M and N). In a similar manner, a pronounced TOP1 expression was also evident in the active lesion areas of MS brains defined by HLA-DR staining of immune cells (Fig 2P).

By exploring public genomic datasets, we determined that under physiological conditions, microglia/myeloid cells have higher baseline expression of *TOP1* compared with other cell types in the adult CNS (Appendix Fig S1A and B). Human monocyte-derived macrophages also upregulate TOP1 expression when stimulated with LPS or IFN- $\alpha$  for 7 h, with a return to baseline levels already 24 h post-challenge (Appendix Fig S1C). In an MS cohort, the peri-lesion normal-appearing white matter (NAWM) had higher *TOP1* expression compared with the healthy control white matter (Appendix Fig S1D). In a sporadic ALS cohort, patients also had increased *TOP1* expression in the anterior horn fraction (enriched for glial cells) compared with healthy controls, but this was not a prominent feature in the neuronal fraction (Appendix Fig S1E). Taken together, these results indicate that increased TOP1 expression is characteristic of several neuroinflammatory conditions and TOP1 may serve as a potential target for controlling neuroinflammation.

### TOP1 inhibition dampens inflammatory responses in stimulated microglia

To evaluate the anti-inflammatory effect of TOP1 inhibition, we first investigated the cytotoxicity of CPT on inflammatory microglia and

a concentration below 1  $\mu\text{M}$  showed no deleterious effect (Fig 3A). We therefore used 1  $\mu\text{M}$  CPT for subsequent *in vitro* experiments (Fig 2A). Pro-inflammatory activated microglia release cytotoxic molecules such as pro-inflammatory cytokines and produce nitric oxide (NO) via the catalytic activity of inducible nitric oxide synthase (iNOS), which can damage CNS neural tissue (Lepka *et al*, 2017). CPT incubation significantly inhibited the release of NO from stimulated microglia (Fig 3B), which was also confirmed by a decreased iNOS immunostaining (Fig 3C and D). Following CPT incubation, the mRNA expression of inflammatory genes *Nos2*, *Tnfa*, and *Il1b* displayed a kinetic change. *Il6* was inhibited by CPT at 1 h, but the kinetic expression pattern was similar to that of the control group (Fig 3E). Conversely, the mRNA expression of the anti-inflammatory cytokine IL-10, which is important for inflammation resolution and maintenance of microglial homeostasis, was highly upregulated after 24 h in CPT-treated LPS/IFN $\gamma$ -stimulated microglia.

We then measured the cytokine release in the supernatants from activated microglia after 24 h. The production of TNF, IL-6, and the monocyte chemoattractant protein CCL2 was reduced in CPT-treated microglia, whereas IL-10 production was significantly increased (Fig 3F). This is in line with a previous study also showing that TOP1 inhibition augments IL-10 production (Yang *et al*, 2019). An increased intracellular TNF synthesis in stimulated microglia was also confirmed by cytokine staining using flow cytometry, and CPT treatment also inhibited the synthesis of this cytokine (Fig 3G and H). Taken together, TOP1 inhibition regulates the inflammatory responses in microglia.

### The FDA-approved TOP1 inhibitor topotecan ameliorates LPS-induced neuroinflammation

Given the effect of CPT on dampening microglia inflammatory responses *in vitro*, we next assessed the effect of TOP1 inhibition *in vivo*. Due to the poor solubility of CPT in saline, we used topotecan (TPT), which is a water-soluble analog of CPT, for *in vivo*

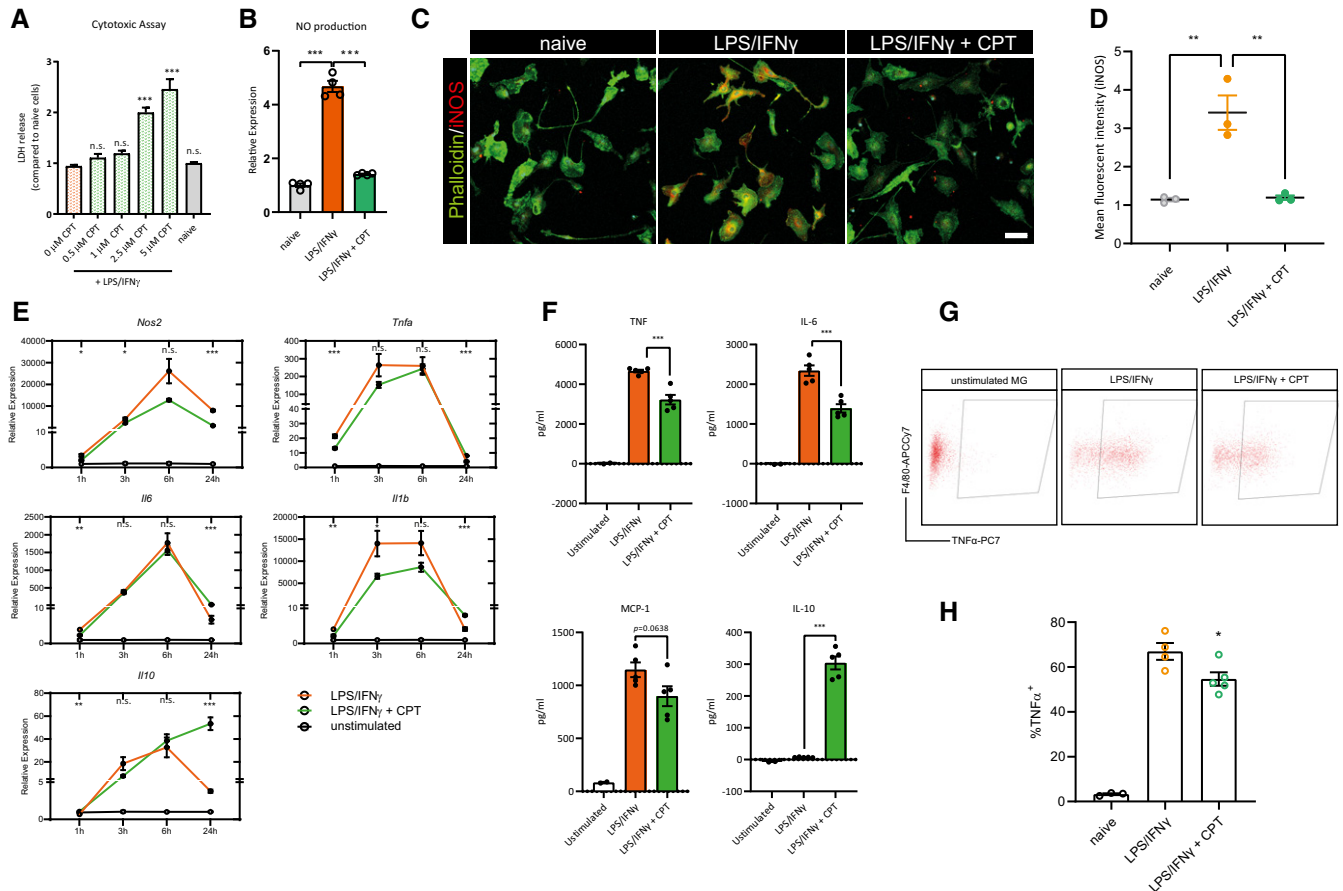


**Figure 3. Camptothecin impedes the inflammatory response in stimulated primary microglia.**

A Cytotoxicity of CPT on stimulated microglia was determined by measuring the release of LDH in the supernatants ( $n = 4$  technical replicates).  
 B Supernatants were collected after 24 h LPS/IFN $\gamma$  stimulation and measured for nitrite, as an index of nitric oxide (NO) production ( $n = 4$  technical replicates).  
 C, D Immunostaining of iNOS (red) and Phalloidin (green) in microglia ( $n = 3$  technical replicates with more than 5 random fields per well) (bar = 50  $\mu$ m).  
 E The kinetics of mRNA expression of *Nos2*, *Tnfa*, *Il1b*, *Il6*, and *Il10* after 1, 3, 6, and 24 h of LPS/IFN $\gamma$  stimulation ( $n = 3$ –6 technical replicates).  
 F Cytokine release (TNF, IL-6, MCP-1, and IL-10) to the supernatants were measured by cytometric beads assay after 24 h LPS/IFN $\gamma$  stimulation ( $n = 2$  or 5 technical replicates).  
 G, H The production of TNF- $\alpha$  within microglia was determined by flow cytometry ( $n = 3$  to 5 technical replicates).

Data information: Data shown are mean  $\pm$  SEM. \* $P < 0.05$ ; \*\* $P < 0.01$ ; \*\*\* $P < 0.001$ ; n.s. = no statistical significance. Statistical analyses were performed using one-way ANOVA with Dunnett's Multiple Comparison Test for (A), (B), and (D), and the comparisons between the LPS/IFN $\gamma$  and LPS/IFN $\gamma$ +CPT group in (E–H) were performed using the student's unpaired two-tailed t-test.

experiments. TPT was approved by FDA in 2007 for the treatment of small-cell lung cancer via oral administration. Similar to CPT, TPT treatment also mitigated inflammatory responses in microglia (Appendix Fig S2A–C) and macrophages *in vitro* (Appendix Fig S2D).

We delivered 10  $\mu$ l TPT (0.1 mg/kg) directly into the CNS via intracisternal injection, followed by 5 mg/kg LPS challenge (i.p), and analyzed the brain tissue after 4 or 24 h (Fig 4A). The expression of Iba1, whose immunoreactivity increases following microglial activation, was enhanced in different brain regions upon LPS treatment, whereas TPT-treated mice exhibited a reduced Iba1 immunoreactivity (Fig 4B–D).

Microglia rapidly adapt their morphology following activation. Resting microglia are ramified cells with many intersections connecting a complex branching network, whereas activated

microglia retract their long processes and become less ramified (Fernández-Arjona *et al*, 2017). We analyzed the morphological status of microglia using *Sholl* analysis (Norris *et al*, 2014), and as expected, LPS challenged mice had a typical amoeboid-like microglia morphology, while those receiving TPT treatment had an intermediate microglial morphology with increased intersections, more ramifications, and longer processes (Fig 4E–I), indicating a less activated state. This was also reflected by a reduction in the mRNA expression of inflammatory genes in the hippocampus and hypothalamus (Fig 4J and K). TPT treatment also resulted in a general reduction in pro-inflammatory cytokine levels compared with the LPS control group as evaluated by cytokine arrays of the brain homogenates (Fig 4L and M). In addition, we also noted a better performance in the explorative behavioral test following TPT treatment (Fig 4N), reflecting less depression-like sickness behavior.

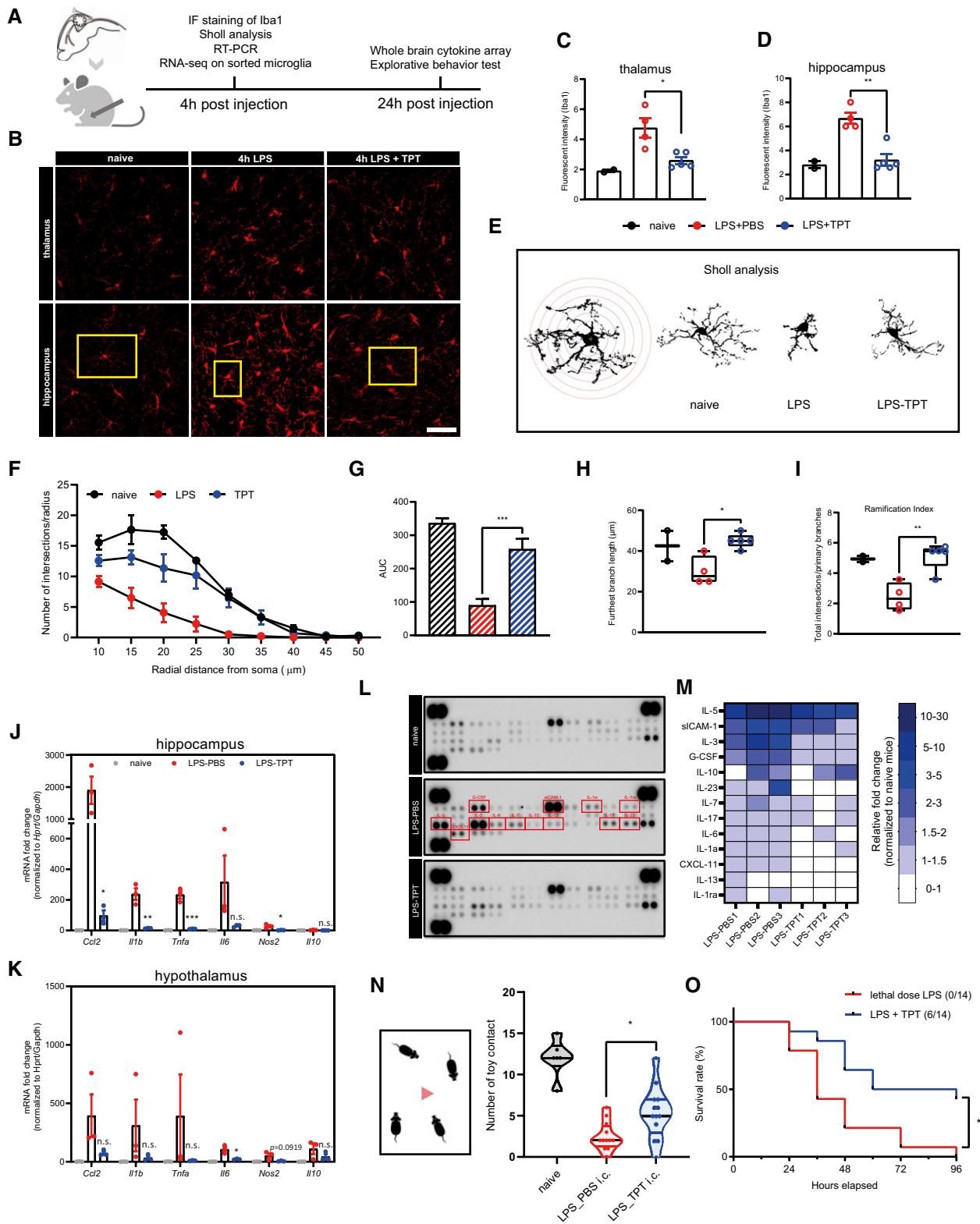


Figure 4.

A previous study reported that CPT rescued mice from a lethal LPS challenge (Rialdi *et al*, 2016). Similarly, we determined that a single low-dose injection of TPT (1 mg/kg) could also prevent around

40% of mice from death induced by lethal inflammation (Fig 4O). Together, these results confirmed the protective effect of TPT on neuroinflammation induced by the LPS challenge.

**Figure 4. Topotecan mitigates microglial activation and CNS inflammation in LPS-challenged mice.**

- A An overview of the experimental design.
- B Microglia in the hippocampus and thalamus were stained with Iba1 (red); bar = 50  $\mu\text{m}$ ; microglia in the yellow boxes were presented in (E).
- C, D Fluorescent intensity of Iba1 in hippocampus and thalamus in (B);  $n = 2, 4, 5$  mice for naive, LPS, and LPS + TPT group, respectively (2–6 sections per mouse were analyzed).
- E *Sholl* analysis was performed to analyze the morphology of microglia. Microglia marked in yellow boxes in (B) were presented accordingly.
- F–I The morphological changes of microglia were objectified by the number of intersections per radius (F and G), furthest branch length (H), and the ramification index presented as total intersections/primary branches (I);  $n = 2, 4, 5$  mice for naive, LPS, and LPS + TPT group, respectively (4–7 complete microglia from each mouse were included for analysis); in (H) and (I), the central band represents the median value, the box extends from the 25<sup>th</sup>–75<sup>th</sup> percentiles, and the whiskers plot the smallest and the largest value.
- J, K Expression of inflammatory genes in the hippocampus and hypothalamus 4 h after the LPS challenge ( $n = 3$  mice).
- L, M Cytokine array on brain homogenates after 24 h of LPS challenge ( $n = 2$  mice for the naive group;  $n = 3$  mice for the LPS and LPS + TPT groups).
- N The contact frequency of each mouse to the new toy during the cage explorative experiment was recorded for 5 min ( $n = 5, 12, 13$  mice for the naive, LPS\_PBS, and LPS\_TPT groups, respectively); data are pooled from two independent experiments with similar results.
- O A lethal dose of LPS (18 mg/kg; i.p.) was given to mice; mice in the LPS + TPT group received 1 mg/kg TPT (i.p.) 1 h before the lethal dose LPS challenge, whereas the control group received PBS injection ( $n = 14$  mice).

Data information: Data shown are mean  $\pm$  SEM. \* $P < 0.05$ ; \*\* $P < 0.01$ ; \*\*\* $P < 0.001$ ; n.s. = no statistical significance. Statistical analyses comparing the LPS\_PBS group with the LPS\_TPT group were performed using the Student's unpaired two-tailed *t*-test; the survival curve was analyzed with Log-rank.

### TPT drives an altered transcriptional phenotype in microglia of LPS-challenged mice

The beneficial effect of TPT in the LPS model prompted us to further characterize the cellular and molecular responses in microglia following TPT treatment. To understand the molecular changes, we sorted microglia 4 h after the LPS challenge and performed RNA sequencing. The multidimensional scaling (MDS) analysis clearly separated the naive control from the LPS (LPS + PBS) and TPT (LPS + TPT) group (Fig 5A). We observed that microglial homeostatic genes (*P2ry12*, *Tmem119*, *Siglech*, *Olfml3*) were significantly downregulated, indicating an immediate microglial activation after the LPS challenge (Fig EV1A). As expected, we confirmed molecular signatures (IL-17, MAPK, NF- $\kappa$ B, TNF, and Toll-like receptor signaling pathways) indicative of activated inflammatory responses in microglia of LPS-challenged mice (Fig EV1B–D).

We next examined differences in gene expression between the TPT and LPS groups. Although LPS caused global gene expression changes in microglia, the TPT group was still distinct from the LPS group according to the MDS analysis, with 327 differentially expressed genes identified (Fig 5A). Among the top 50 downregulated genes following TPT treatment, many are key regulators controlling inflammatory responses in microglia, such as *Cebpd*,

*Mmp14*, *Hdac2*, and *Junb* (Fig 5B and C). The expression of *Cebpb*, *Mmp14*, and *Hdac2* was also significantly increased in the LPS group when compared with the naive group (Fig EV1A). We also noted that several small GTPase genes (*Rab5a*, *Rab5if*, *Rab10*, *Rab24*) were significantly downregulated. Many of these genes are involved in endosomal pathways and intracellular vesicle trafficking, which are processes important for cytokine transportation and release. In addition, we noted that the inflammatory pathways activated following the LPS challenge were significantly inhibited in the TPT group, including TNF and NK- $\kappa$ B signaling pathways, which further corroborated our findings of a potent anti-inflammatory and protective effect of TPT in activated microglia and LPS challenged mice (Figs 5D–F and EV1E–H).

In addition to suppression of many inflammatory pathways following TPT treatment, transcripts of oxidative phosphorylation, steroid biosynthesis, and mitochondrial respiratory activities were enriched, indicating a potential metabolic reprogramming in microglia (Fig 5G and H). We also predicted the potential transcription factors (TFs) mediating TPT effects using Binding Analysis for Regulation of Transcription (BART) and Hypergeometric Optimization of Motif Enrichment (HOMER) analysis. From the ChIP-seq data-based BART analysis, we obtained 90 predicted TFs, and among those, eight were differentially expressed when comparing the TPT and

**Figure 5. Topotecan reshapes the transcriptional profile of microglia after systemic LPS challenge.**

- A Multidimensional scaling (MDS) analysis of brain microglia sorted from the following groups ( $n = 3$ ): naive group (mice received i.p. injection of PBS and intracisternal injection of PBS), LPS group (mice received i.p. injection of 5 mg/kg LPS following intracisternal injection of PBS), and TPT group (mice received i.p. injection of 5 mg/kg LPS following intracisternal injection of 0.1 mg/kg TPT); numbers labeled between different clusters indicate the number of differentially expressed genes (DEGs) identified by EdgeR ( $FDR \leq 0.05$ ).
- B Volcano plot depicting the DEGs between the TPT and LPS groups; dots represent non-DEGs (grey,  $FDR > 0.05$ ), DEGs with fold change  $\log_2FC > 0$  (red), and DEGs with  $\log_2FC < 0$  (blue); genes of interest were labeled and plotted in darker colors.
- C Bar plot of the top 50 up- and downregulated DEGs (ordered by FC) between the TPT and LPS groups.
- D GSEA plot of the enriched KEGG pathways related to inflammation between the TPT and LPS groups.
- E–H Heatmaps plotting the changes in expression levels of genes contributing to the enrichment analysis of TNF signaling pathway (E) and NF- $\kappa$ B signaling pathway (F) across samples when comparing the TPT group with the LPS group. Dot plots showing the top10 suppressed and activated GO terms (G) or KEGG pathways (H) between the TPT and LPS groups. The expression levels were calculated by TPM and  $\log_2$  transformed.
- I Venn diagrams intersected the number of DEGs and transcription factor (TF) predicted to regulate the gene expression between the TPT and LPS groups.
- J The Scatter plot shows the Irwin-Hall and FDR value of the 8 genes in (I); FDR was obtained from differential expression (DE) analysis; Irwin-Hall *P*-value was obtained from BART prediction, indicating the integrative ranking significance; the color gradient indicates FC in DE analysis.
- K BART output of association score cumulative distribution of *Ikzf1*.
- L BART output of transcriptional regulator prediction rank of *Ikzf1*.
- M *De novo* motif enriched in promoters of DEGs between the TPT and LPS groups matching to known motifs of *Ikzf1* using HOMER.

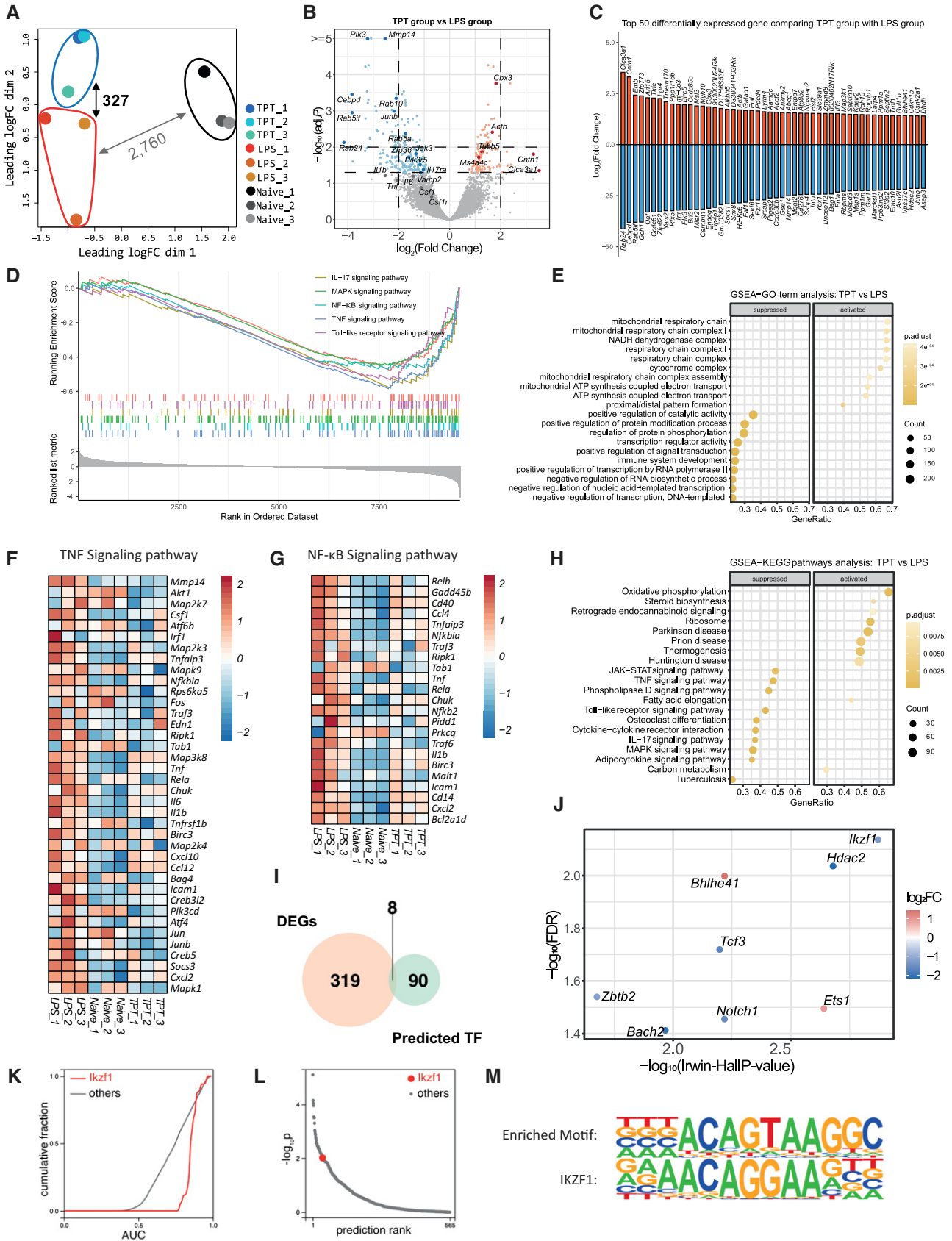


Figure 5.

LPS groups (*Zbtb2*, *Tcf3*, *Notch1*, *Ikzf1*, *Hdac2*, *Ets1*, *Bhlhe41*, *Bach2*) (Figs 5I and J, and EV1I). By combining the confidence of transcription factor prediction (Irwin-Hall p-value) with differential expression analysis, *Ikzf1* ranked the highest (Figs 5J–L and EV1I). Furthermore, the known motif of *Ikzf1* showed high similarity to one of the top-ranked motifs that occurred in the promoter regions of differentially expressed genes (Figs 5M and EV1J). This indicates that TPT may protect microglia against inflammatory activation by downregulating *Ikzf1* which commonly regulates pro-inflammatory gene transcription (Li et al, 2011; Song et al, 2016). *Ikzf1* encodes the transcription factor Ikaros, whose function in microglia is seldom reported. We validated that Ikaros was highly induced in activated microglia, and that TPT could downregulate its expression (Fig EV2A–D); a similar trend was present in the LPS-challenged mice brain (Fig EV2E–G). Taken together, our results reveal a less inflammatory microglia transcriptional phenotype following TPT treatment, with key pro-inflammatory regulators and signaling pathways being remodeled.

### TPT prevents disease progression in experimental autoimmune encephalomyelitis

We next extended our study to the more MS-relevant EAE model for investigation. For testing the effect of TPT in EAE, we employed a treatment protocol comprising 3 injections of TPT (1 mg/kg; i.p) (Fig 6A). This is a much lower dose (5- to 10-fold reduction) compared with previous studies using TPT as a typical chemotherapeutic agent in rodent models and is equivalent to the well-tolerated dose reported in a mouse model of Huntington's disease (Némati et al, 2010; Shekhar et al, 2016; Chernov et al, 2017). We characterized that this treatment protocol did not induce a loss of body weight (Appendix Fig S3A), nor a significant decrease in the number of lymphocytes in the blood (Appendix Fig S3B) and spleen (Appendix Fig S3C–F), excluding the unwanted immunosuppression and cytotoxic effects.

We included three TPT treatment groups: (i) the *pre-onset* group receiving TPT on days 5, 7, and 9 post-immunization; (ii) the *onset* group receiving TPT on days 11, 13, and 15; and (iii) the *peak* group on days 17, 19, and 21. EAE mice gradually lost weight upon disease

onset, but mice in the TPT pre-onset and onset treatment groups experienced less weight loss (Fig 6B). TPT pre-onset treatment significantly delayed EAE disease onset and prevented disease development (Fig 6C–G). Both TPT pre-onset and onset treatment improved the EAE clinical score, while TPT treatment starting from disease peak failed to do so (Fig 6C). Since the day-of-onset for each EAE mouse varied even within the same EAE batch, we then treated the EAE mice individually from the day the mouse was scored 1 for the first time, thereby ensuring that all mice were sick when treatment commenced. We again observed a significant therapeutic effect of TPT in this experimental setting (Fig 6H). We also analyzed the spinal cords on days 18 and 30 and confirmed a reduced infiltration of peripheral monocytes into the spinal cord at EAE peak, and a smaller demyelinated area at the EAE recovery phase following TPT *onset* treatment (Fig 6I–M). Furthermore, we analyzed the functionality of the immune cells in the spinal cords at the EAE peak from the TPT *onset* treatment group and PBS control group. In terms of cytokine production, we noted an increased production of IL-10 in CD11b<sup>+</sup> myeloid cells in TPT-treated mice, whereas TNF- $\alpha$  remained unaltered (Fig EV3A and B). There was no difference in the frequency of Ki67<sup>+</sup> CD4<sup>+</sup> proliferating T cells, and Foxp3<sup>+</sup> CD4<sup>+</sup> regulatory T cells (Fig EV3C and D), and we did not observe a difference in GM-CSF and IFN- $\gamma$  production of CD4<sup>+</sup> T cells between the two groups (Fig EV3E and F). These results, together with the effect of TPT in the LPS challenge model, led us to conclude that TPT could be repurposed for the treatment of neuroinflammatory conditions.

### Bioengineered DNA origami for specific delivery of TPT to myeloid cells

TPT is approved as a chemotherapeutic drug. The long-term application of TPT could lead to indiscriminate DNA damage to all cells. While a low-dose and short-term application of TPT had limited toxicity (Appendix Fig S4A–C), we still aimed for a more specific delivery and restrict both the beneficial and side effects of TPT mainly on the myeloid cells. From a translational perspective, this could even enhance the effect of TPT on myeloid cells, and meanwhile, minimize the potential off-target effects on other cell types when applying TOP1 inhibition therapy in patients. We took advantage of our

**Figure 6. Topotecan prevents disease progression in the EAE model.**

- A Mice received TPT treatment (1 mg/kg; i.p) at indicated days post-immunization and were randomly assigned to the *pre-onset* group (day 5, 7, 9), *onset* group (day 11, 13, 15), and *peak* group (day 17, 19, 21); mice in the EAE control group received 3 PBS injections randomly from day 5 (i.p).
- B Bodyweight change following EAE immunization ( $n = 9–11$  mice per group).
- C–G EAE clinical scores among the groups were analyzed using different parameters: area under the curve (C), day of onset (D), cumulative score (E), the average score from day 10 (F), and max score (G);  $n = 9–11$  mice per group; data are from one EAE batch representing three batches with a similar effect.
- H EAE mice were treated individually from the day when they were just scored or scored higher than 1;  $n = 8$  mice per group. Data are from one EAE batch representing two batches with a similar effect.
- I EAE mice from the *onset* group or control were euthanized at the peak of EAE (day 18), and the spinal cords were dissected for flow cytometry with an antibody panel for myeloid cells.
- J The counts of different myeloid cells in (I), including monocytes (Mono), macrophages (Mac), microglia (Mic), and neutrophils (Neutro), were graphed ( $n = 5$  mice); this experiment was performed twice.
- K Spinal cord sections dissected from Day 30 from the EAE batch in (H) were stained with CD11b (red), Fluoromyelin (green), and Hoechst (blue) (bar = 200  $\mu$ m).
- L The CD11b immunofluorescent intensity in (K) was graphed ( $n = 2$  mice for the control group;  $n = 4$  mice for the EAE-PBS and EAE-TPT groups).
- M The percentage of demyelinated area in the white matter of the spinal cord was graphed ( $n = 2$  mice for the control group,  $n = 4$  mice for the EAE-PBS and EAE-TPT groups).

Data information: Data are presented as the mean  $\pm$  SEM. \* $P < 0.05$ ; \*\* $P < 0.01$ ; \*\*\* $P < 0.001$ ; n.s. = no statistical significance. The following statistical analyses were used as follows: the EAE scores in (D–G) were analyzed using the Kruskal–Wallis nonparametric test; the AUC in (C) was analyzed using the one-way ANOVA with Dunnett's Multiple Comparison test, and the Student's unpaired two-tailed t-test was used for comparing the EAE-PBS group with the EAE-TPT group in H (AUC), J, L, and M.

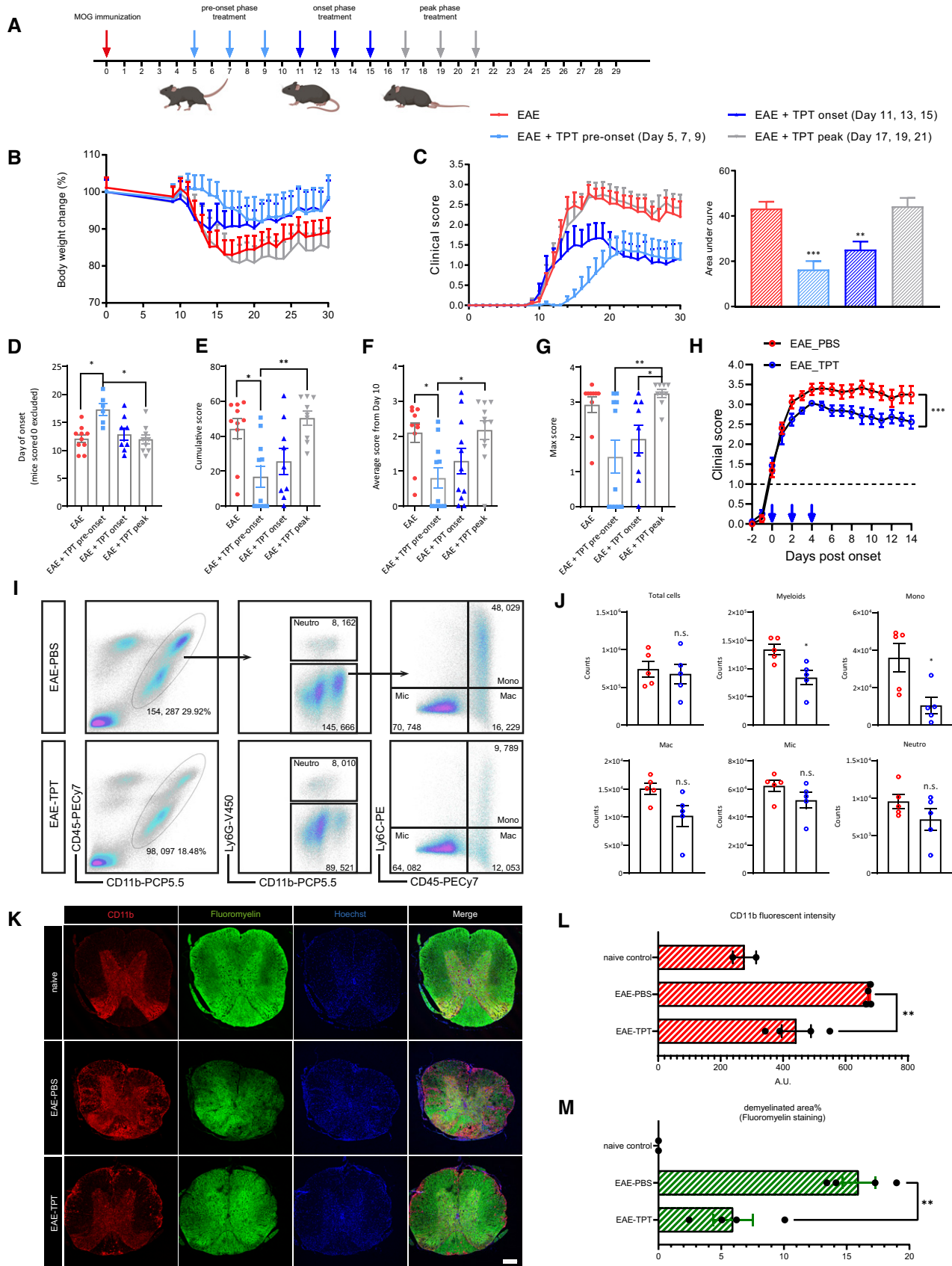


Figure 6.

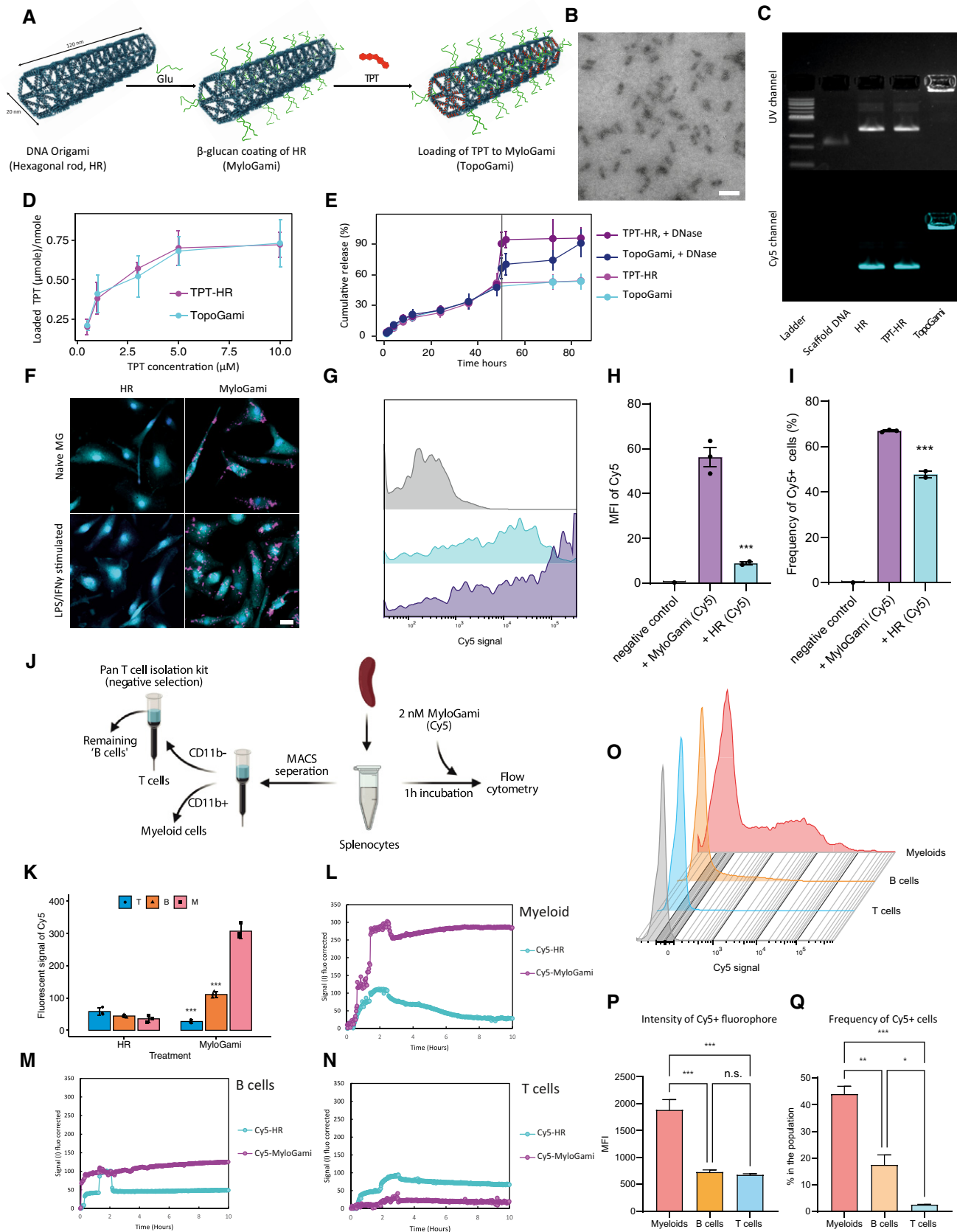


Figure 7.

**Figure 7. A bioengineered DNA-origami nanosystem for selective topotecan (TPT) delivery to myeloid cells.**

- A A hexagonal rod (HR)-structured DNA origami surface-coated by  $\beta$ -glucan (MyloGami) with loaded TPT (TopoGami) for myeloid cell-specific TOP1 inhibition.
- B Ultrastructural confirmation of the HR structure under transmission electron microscopy (bar = 100 nm).
- C Cy5-labelled DNA nanostructures (HR, TPT-HR, and TopoGami) electrophoresis on 2% agarose gel; the gel is pre-stained with ethidium bromide and imaged under the UV channel and Cy5 channel.
- D TPT loading efficacy of HR and MyloGami ( $n = 3$  technical replicates).
- E Cumulative TPT release profiles of TPT-HR and TopoGami with or without DNase adding at the time point 48 h ( $n = 3$  technical replicates).
- F Uptake of Cy5-labelled HR or MyloGami (in magenta) by non-stimulated or stimulated mouse primary microglia (in cyan) after 1 h incubation with 2 nM of the structures (bar = 20  $\mu$ m).
- G–I Flow cytometry analysis comparing the uptake of Cy5-labeled HR or MyloGami in non-stimulated microglia incubated with 2 nM of the structures for 1 h ( $n = 1–3$  biological replicates); the quantification was based on the median fluorescent intensity (MFI) or the percentage of Cy5-expressing cells in total cells.
- J Splenocytes were processed for comparing the uptake of Cy5-labelled MyloGami in different immune cells. The cells were separated using magnetic-activated cell sorting (MACS) into 3 compartments (myeloid cells, T cells, and B cells) for subsequent LigandTracer experiments in (K–N), or directly incubated with Cy5-labelled MyloGami for flow cytometry analysis (O–Q).
- K The fluorescent signal of Cy5 in different immune cell compartments after 8 h incubation with HR or MyloGami in LigandTracer experiments; T for T cells, B for B cells, and M for myeloid cells; data are pooled from three observations.
- L–N The real-time interaction of Cy5-labelled HR or MyloGami to myeloid cells (L), B cells (M), and T cells (N). 2 nM of structures were added to the cells at 0 h, and 6 nM of structures were added to the cells at 1 h; the unbonded structures were removed after 2–3 h and the cells were kept in a fresh medium afterward.
- O–Q Flow cytometry analysis of Cy5 fluorescent signal in CD11b<sup>+</sup>CD45<sup>+</sup> myeloid cells, CD11b<sup>−</sup>CD45<sup>+</sup>CD19<sup>−</sup>CD3<sup>+</sup> T cells, and CD11b<sup>−</sup>CD45<sup>+</sup>CD19<sup>+</sup>CD3<sup>−</sup> B cells; the quantification was based on the median fluorescent intensity (MFI) or the percentage of Cy5-expressing cells in each population ( $n = 3$  biological replicates).
- Data information: Data are presented as the mean  $\pm$  SEM. \* $P < 0.05$ ; \*\* $P < 0.01$ ; \*\*\* $P < 0.001$ ; n.s. = no statistical significance. The statistical analyses were performed using the Student's unpaired two-tailed t-test (H and I), and one-way ANOVA with Dunnett's Multiple Comparisons Test (K) or Tukey's Multiple Comparisons Test (P and Q).

previously designed wireframe-stylized hexagonal rod (HR) DNA origami system (Benson *et al*, 2015; Wang *et al*, 2021). The superiority of using DNA origami as a drug delivery vehicle is the precision and reproducibility (Rothmund, 2006; Douglas *et al*, 2012). Unlike other self-assembled nanoparticles that often have a relatively broad size distribution, DNA origami has the same controlled shape, size, and charge for each particle. The HR used in this work had a length of  $\sim 120$  nm and a diameter of  $\sim 20$  nm (Fig 7A). To enhance specificity to myeloid cells, we surface-modified the HR with  $\beta$ -glucan, which is a ligand from baker's yeast recognized mainly by the Dectin-1 receptor expressed on myeloid cells (Aouadi *et al*, 2009). To coat HR with  $\beta$ -glucan, we designed 60 evenly distributed protruding single-stranded DNAs around the HR for the hybridization of single-stranded polyA50 containing DNA oligos. One polyA50 oligo and two glucan polymers can then form a stable triple-helical conformation at the site where polyA50 is located on HR (Sakurai *et al*, 2005; Sanada *et al*, 2012), forming glucan-coated HR (HR-Glu, or denoted as MyloGami). Previous studies have revealed that TPT binds to single-stranded nicks in double-stranded DNA (dsDNA) through which it stops topoisomerase to correct the overwinding or underwinding of DNA during DNA replication and transcription (Staker *et al*, 2002; Bocian *et al*, 2008). TPT could also intercalate between the bases in dsDNA (Joshi *et al*, 2014). These interactions between TPT and dsDNA thus enabled the loading of TPT into the DNA origami nanostructure without chemical conjugation.

We loaded TPT into MyloGami and denoted this system TopoGami. We confirmed the expected hexagonal rod structure of TopoGami by transmission electron microscopy (Fig 7B). Agarose gel electrophoresis of Cy5-labeled HR, TPT-HR, and TopoGami revealed that all samples had sharp-structured bands, indicating the high quality and consistency of structure production irrespective of TPT loading. More importantly, TopoGami migrated poorly during electrophoresis, reflecting the fact that the structure was successfully coated by glucan as it neutralized the negatively charged DNA (Fig 7C). We determined that the saturated TPT loading capacity in 1 nM of HR was  $\sim 600$  nM, and glucan coating had no effect on the

loading efficiency (Fig 7D). We also characterized the stability of the drug-loading DNA origami structure by measuring the cumulative TPT release overtime. The release profile of TPT revealed no sudden increase within 84 h, indicating the stable integration between TPT and the DNA nanostructure. However, when we added DNase, we observed that TPT release from TopoGami accelerated gradually, whereas the release from the TPT-HR DNA origami without glucan coating surged immediately (Fig 7E). This differential sensitivity to DNase thus suggested that  $\beta$ -glucan coating, in addition to acting as a myeloid-binding ligand, can also protect the DNA nanostructure from protein accessibility and therefore prevent its degradation.

To confirm glucan-mediated enhanced internalization of the DNA structure to myeloid cells, we incubated mouse primary microglia with 2 nM HR or MyloGami in both resting and activated states for 1 h. MyloGami was efficiently taken up by microglia compared with HR, irrespective of microglial activation state (Fig 7F). This was further demonstrated by flow cytometry as an increased Cy5 fluorophore intensity was observed in microglia treated with MyloGami compared with those exposed to HR (Fig 7G–I).

We next assessed the binding specificity of MyloGami to different immune cells using splenocytes as a source. We separated the splenocytes into three major immune compartments (myeloid cells, T cells, and B cells) and performed a real-time structure-to-cell interaction assay in each compartment (Fig 7J). All the 3 cell compartments had limited interactions with the non-coated HR (Cy5-labelled), but the interaction between the Cy5-labeled MyloGami and myeloid cells was much higher than that of the B and T cells (Fig 7K–N). To further validate these findings, we incubated splenocytes with Cy5-labeled MyloGami and performed flow cytometry (Fig 7J). We gated for the 3 cell types (Appendix Fig S5) and again observed a significantly increased uptake of the Cy5-labelled MyloGami in the myeloid compartment (Fig 7O–Q). In addition, MyloGami uptake was also evaluated *in vivo*. We performed kinetic fluorescence imaging (IVIS) of mice receiving i.v. injection of Cy5, HR-Cy5, or MyloGami-Cy5, respectively, and noted a clear difference in the distribution pattern of Cy5 fluorescence signal in the

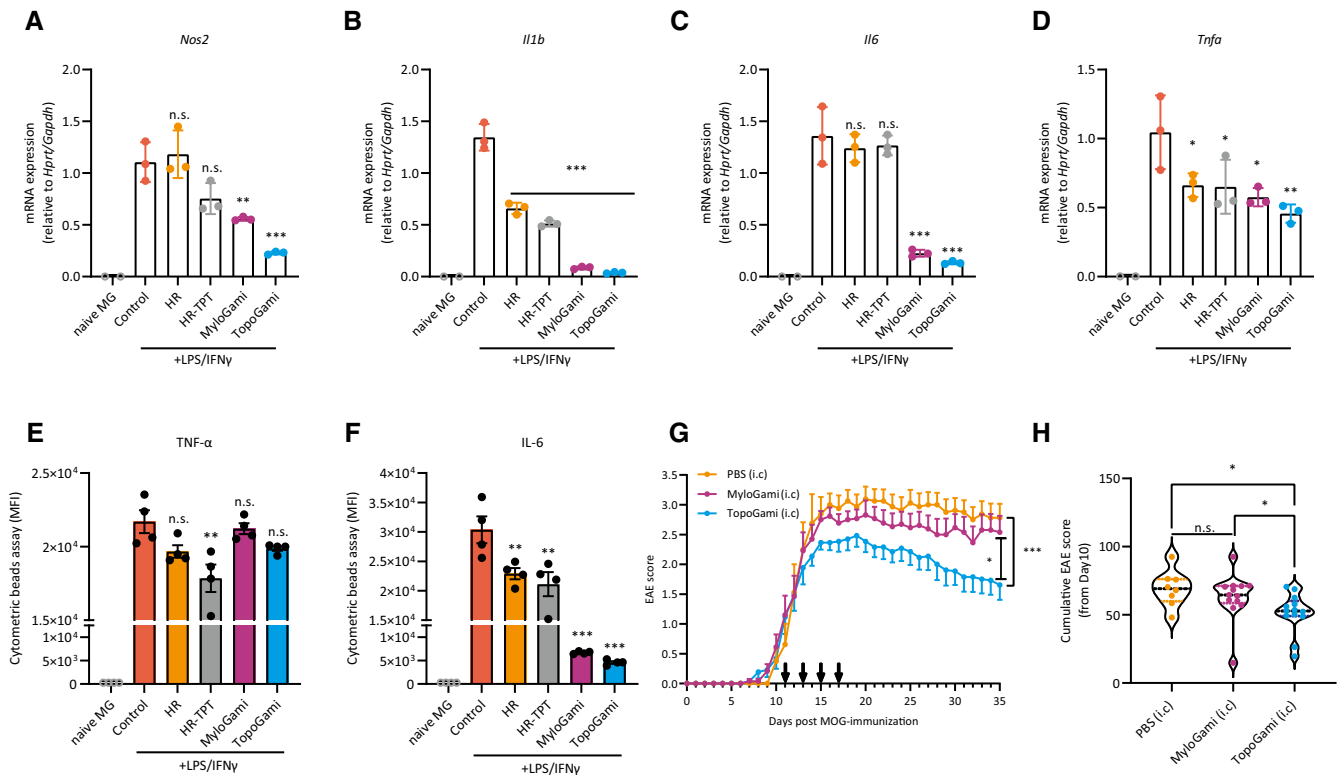


**Figure 8. TopoGami inhibits the inflammatory responses in stimulated microglia and ameliorates EAE.**

A–D The mRNA expression of *Nos2*, *Il1b*, *Il6*, and *Tnfa* in microglia treated with HR, TPT-HR, MyloGami, or TopoGami after 4 h LPS/IFN $\gamma$  stimulation ( $n = 3$  technical replicates). E, F The cytokine release of IL-6 and TNF- $\alpha$  from microglia treated with HR, TPT-HR, MyloGami, or TopoGami after 24 h LPS/IFN $\gamma$  stimulation were measured by cytometric beads assay ( $n = 4$  technical replicates). G, H Mice with EAE received intracisternal injections of TopoGami, MyloGami, or PBS, on days 11, 13, 15, 17 post-immunization ( $n = 8$  mice for the PBS group;  $n = 13$  mice for the TopoGami and MyloGami groups).

Data information: Data are presented as the mean  $\pm$  SEM. \* $P < 0.05$ ; \*\* $P < 0.01$ ; \*\*\* $P < 0.001$ ; n.s. = no statistical significance. Statistical analyses for (A–F) and the AUC in (G) were analyzed using one-way ANOVA with Dunnett's Multiple Comparison test; Kruskal-Wallis nonparametric test was performed for EAE cumulative score in (H).

MyloGami-injected mice compared with that in the HR-injected mice. There was a rapid accumulation and prolonged retainment in the liver and potentially also the abdominal adipose tissue as previously reported using other fluorescent-conjugated glucan particles (Fig EV4A) (Aouadi *et al*, 2013; Sharma *et al*, 2019). Although the spleen is not a major organ for glucan particle accumulation (Sharma *et al*, 2019), we still noted an increase of Cy5 signal in the myeloid cells, but not in other immune cells (Fig EV4B). We also identified Cy5-MyloGami accumulation in liver F4/80 $^+$  macrophages 6 h after injection (i.p), but this was not evident in the kidney (Fig EV4C and E). When delivered to the CNS via intracisternal injection, MyloGami colocalized with microglia/macrophages in the CNS after 3 h (Fig EV4D). Taken together, these results indicate that MyloGami is a stable delivery system for enhanced targeting of myeloid cells, and that TopoGami could be a myeloid cell-specific means of inhibiting TOP1.

#### TopoGami recapitulates the anti-inflammatory effects of TPT

We next verified the anti-inflammatory properties of TopoGami. We harvested microglia after 4 h stimulation and performed RT-PCR analysis of inflammatory genes. Compared with the control group,

TopoGami strongly inhibited the mRNA expression of *Nos2*, *Il1b*, *Il6*, and *Tnfa* (Fig 8A–D). We also analyzed cytokine release in the supernatants from treated cells after 24 h, and TopoGami significantly inhibited the release of IL-6 and reduced TNF- $\alpha$  production to a large extent (Fig 8E and F). Previous studies have reported that DNA nanostructures *per se* could inhibit inflammatory responses in macrophages treated with LPS/IFN $\gamma$  (Zhang *et al*, 2018). In accordance with this, we also noted that HR exhibited a certain degree of anti-inflammatory properties. This was more obvious in MyloGami, possibly due to enhanced delivery of HR into the cells due to  $\beta$ -glucan coating (Fig 7F). Nevertheless, with the addition of TPT, TopoGami had a greater inhibitory action due to the synergistic effects of both the DNA nanostructures and of TPT.

To assess the ability of TopoGami to ameliorate neuroinflammation, we employed the EAE model. We first administered TopoGami with 100  $\mu$ M loaded TPT (100  $\mu$ l per mouse) via i.p injection on days 5, 7, and 9 after immunization as a prophylactic treatment. Similar to results with TPT itself, i.p injection of TopoGami also delayed EAE progression (Fig EV5A and B). We then assessed if targeting microglia and infiltrating inflammatory myeloid cells in the CNS alone could confer beneficial effects. Therefore, we delivered 10  $\mu$ l TopoGami directly into the CNS via intracisternal

injection from the EAE onset phase (injected at days 11, 13, 15, and 17 post-immunization). TopoGami treatment significantly improved the clinical symptoms compared with both the PBS group and the MyloGami group (Fig 8G and H). These results demonstrate that targeting myeloid cells using the myeloid cell-specific TOP1 inhibitor TopoGami mitigates microglial activation and MS-like disease.

## Discussion

The importance of myeloid cells in neuroinflammatory conditions has been acknowledged greatly in recent years. Other than depleting myeloid cells using CSF1R inhibitors, preclinical therapeutics regulating myeloid cell function are scarce. Based on this status quo, the purpose of our study was to discover novel therapeutics that regulate dysfunctional myeloid cells (particularly microglia) and to develop practical drug delivery tools to potentiate the specific targeting of myeloid cells. Several landmark studies have highlighted TOP1 inhibition as a strategy for virus infection-induced inflammation, with a recent study reporting that TPT suppresses lethal inflammation induced by SARS-CoV-2 in hamsters (Rialdi et al, 2016; Ho et al, 2021). Serendipitously, we independently identified TOP1 inhibitors as potent anti-inflammatory agents for inflammatory microglia and demonstrated their efficacy in treating neuroinflammatory diseases. Importantly, we designed a novel bioengineered TOP1 inhibitor (TopoGami) that could efficiently and specifically target myeloid cells and reduce their pro-inflammatory activation state.

We screened a list of compounds with underlying microglia-modulating functions using *Connectivity Map*. Apart from camp-tohecin, the high rank of mitoxantrone on the list is also noteworthy. Mitoxantrone was originally developed as an antineoplastic drug but was repurposed and approved for use in relapsing-remitting MS and aggressive progressive MS (Hartung et al, 2002; Foo et al, 2020). Although the mechanism of mitoxantrone in treating MS was not fully elucidated when it was approved, it has been determined to inhibit microglial inflammatory responses by antagonizing TLR4 and suppressing downstream NF- $\kappa$ B activation (Rinne et al, 2020). Not only does this validate our screening strategy, but our screened drug lists also provide insights into the development of future therapeutics for neuroinflammation.

Our transcriptome profiling from sorted microglia following the LPS challenge treated with or without TPT provides robust information regarding the mechanism of action of TPT in activated microglia. First, among the top pathways from our GSEA analysis, several fundamental inflammatory pathways were significantly suppressed by TPT treatment, accompanied by the downregulation of many inflammatory genes. This further substantiated our data showing the effective anti-inflammatory property of TPT in inflammatory microglia and neuroinflammatory conditions in LPS and EAE models. Second, our GSEA analysis also revealed metabolic reprogramming in microglia following TPT treatment. We determined the activation of pathways related to the mitochondrial respiratory chain, oxidative phosphorylation (OXPHOS), and steroid biosynthesis. Steroids have been shown to hinder the induction of pro-inflammatory cytokines in microglia and exert anti-inflammatory effects via ADIOL-ER $\beta$ -CtBP gene transrepression pathway (Saijo et al, 2011). And it has also been well-documented

that a metabolic shift of microglia from glycolysis to OXPHOS with more oxygen consumption underlies the phenotypic change from a pro-inflammatory state to an immunoregulatory state, or a return to the homeostatic state (Bernier et al, 2020; Lauro & Limatola, 2020). In addition, we also predicted potential transcription factors through which TPT could regulate downstream inflammation-related gene expression. Among these, *Ikzf1* is very intriguing. Ikaros (encoded by *Ikzf1*) was initially identified as a lymphoid-specific transcription factor, and its function in myeloid cells, especially in microglia, is under-appreciated (Francis et al, 2011). Several studies have examined the role of Ikaros in macrophages, but the results revealed distinct functions of Ikaros (Cho et al, 2008; Li et al, 2011; Sung et al, 2014; Oh et al, 2018a; Mougiakakos et al, 2021). We report that Ikaros is highly involved in microglial activation and could be a potential downstream target of TPT, but this warrants further investigation.

TPT treatment initiated at the peak of EAE failed to ameliorate clinical neurological signs of disease. We consider that during the EAE recovery phase in the C57BL/6 strain, the infiltration of immune cells and progressive inflammation has retreated, while oligodendrocyte precursors proliferate at a high pace and differentiate into mature oligodendrocytes to repair demyelinated nerves. TPT treatment during this phase is not effective in this less inflammatory context but may affect cell proliferation and subsequent remyelination (Brehm et al, 2001). Coincidentally, a very recent study using a network-based deep learning algorithm developed for novel drug target identification and *in silico* drug repurposing also predicted that TPT is an effective inhibitor of ROR $\gamma$ t and thus, may ameliorate EAE (Zeng et al, 2020). In this study, they treated EAE mice from disease onset with TPT using a relatively high dose (10 mg/kg; i.p) and observed a protective effect. However, as TPT is a chemotherapeutic drug, with this high dose, it is hard to distinguish if the effect is simply due to an overall immunosuppression/cytotoxicity on the highly proliferating immune cells. In our study, we used a much lower dose (1 mg/kg; i.p) and confirmed that our treatment regime did not induce cytotoxicity in naive mice. Furthermore, we also proved that inhibiting TOP1 only in CNS myeloid cells using TopoGami can improve EAE. At the same time, in addition to the *in vitro* validation of increased TOP1 expression in inflammatory microglia, we characterized an increased TOP1 expression in different neuroinflammatory contexts. To our knowledge, our study is the first to indicate an altered TOP1 expression in neuroinflammatory settings.

The *in vivo* application of classical compact, lattice-based DNA origami nanostructures has been hindered by two main challenges. First, stabilization of this type of DNA origami nanostructures usually needs divalent cations, such as Mg<sup>2+</sup>, at the milli-molar range to overcome the electrostatic repulsion between closely packed DNA phosphate anions (Ponnuswamy et al, 2017). This causes poor structural stability in physiological fluids which do not contain such a high concentration of cations. Second, bare DNA origami nanostructures would be rapidly cleared *in vivo* by nucleases (Cassinelli et al, 2015). Thus, for reliable biomedical applications, the stability of DNA origami nanostructures under physiological conditions must be ensured. Our wireframe-stylized HR used in the work, due to its much lower DNA packaging density, has the advantage of cation independence. Recently, polymer protection strategies, such as oligolysine-PEG and cationic poly (2-dimethylamino-ethyl

methacrylate, or PDMAEMA), have shown potential in stabilizing DNA origami nanostructures from nuclease degradation (Kiviahio *et al.*, 2016; Ponnuswamy *et al.*, 2017). However, these polymers are not expected to possess any other biological functions. We now for the first time used  $\beta$ -glucan to coat DNA origami nanostructures. This represents a “two-birds-with-one-stone” strategy achieving both the Dectin-1 receptor targeting on myeloid cells and the protection of DNA origami nanostructures to nucleases.

The construction and application of DNA origami-based TopoGami enabled us to localize the effect of TPT on myeloid cells. Recent studies have noted that although DNA nanostructures can induce inflammatory responses in resting macrophages, they also significantly inhibit the inflammatory response in macrophages treated with LPS/IFN $\gamma$  (Zhang *et al.*, 2018; Zhao *et al.*, 2020; Ma *et al.*, 2021). Consistent with this, we observed that the DNA origami constructs (HR and MyloGami) as vectors themselves could decrease inflammatory cytokine production to a certain degree in activated microglia. MyloGami had an even better effect compared with HR. This could be ascribed to enhanced delivery of the DNA nanostructures into the cells, rather than the effect of the  $\beta$ -glucan coating, as the concentration of  $\beta$ -glucan we used to modify HR was quite low, and low concentrations of  $\beta$ -glucan may not induce significant immunological responses (Xu *et al.*, 2016). Despite the anti-inflammatory effect of MyloGami in inflammatory activated microglia *in vitro*, when we applied TopoGami and MyloGami in the EAE model, we only observed a reduced EAE score in the TopoGami-treated group. We speculate that in the context of EAE, the CNS myeloid cells, unlike those homogeneously activated by LPS/IFN $\gamma$  *in vitro*, are quite heterogeneous and may exhibit variable activation states (Jordão *et al.*, 2019). MyloGami may attenuate the inflammatory response of the activated myeloid cells, but also induce activation of other myeloid subsets in more quiescent states. This may explain why MyloGami only had some beneficial effects in cultured cells, but not *in vivo* in the EAE model. Interestingly, in accordance with this speculation, we even noted a slightly earlier EAE disease onset in mice receiving MyloGami as a prophylactic treatment (starting from Day 5 post-immunization), when most myeloid cells are not yet inflammatory activated (Fig EV5).

An unfulfilled challenge for future work is to modify MyloGami/TopoGami to pass through the blood-brain barrier, even though its integrity in patients with neuroinflammation is disrupted. Although MyloGami targets myeloid cells, under neuroinflammatory conditions such as in the context of demyelination in MS, resident microglia and infiltrating monocytes/macrophages may have distinct roles (Yamasaki *et al.*, 2014), and thus a more specific targeting of different myeloid subsets with further refined surface modification of DNA origami will be even more valuable. Additional validation of TPT or TopoGami in other neuroinflammatory models such as the SOD1-G93A mice of ALS would further add support to our findings. Last, we briefly unveiled the potential involvement of *Ikzf1* in microglia following LPS stimulation and TPT treatment, but the exact role of *Ikzf1* in regulating microglial function warrants further studies.

Our study indicates TOP1 inhibition as a promising therapeutic strategy for neuroinflammatory disorders. We not only further confirmed the important role of myeloid cells in neuroinflammatory contexts, but also provided insights and tools for developing

appropriate future therapeutics with a demand to target myeloid cells using MyloGami/TopoGami. For instance, boosting the pro-regeneration property of microglia by loading pro-remyelination agents into MyloGami for better remyelination in MS (Mishra & Yong, 2016). Our study thus will benefit patients with dysfunctional myeloid cells.

## Materials and Methods

### Study design

This study aims to determine the repurposing property of topotecan for the treatment of neuroinflammation with the application of DNA origami to achieve specific delivery to myeloid cells. We followed the ARRIVE guidelines for reporting the use of the research animals. Mouse primary bone-marrow-derived macrophages and primary microglia were used for *in vitro* experiments. The EAE and LPS models were induced for *in vivo* experiments; both adult males and females were tested in different repetitions (no gender difference was observed in terms of the effect of TPT or TopoGami). Mice were randomly assigned to each treatment group; the scoring of EAE mice, and the assessment of the explorative behavior of LPS mice, were performed in a blinded fashion. The sample size was determined by the availability of age-matched mice and previous experience with the EAE model and LPS model, and mice were excluded from the study under the following situations: (i) Mice had other problems and had to be sacrificed according to the veterinarian and the ethical permit, such as a long tooth, fighting and bleeding, rectal prolapse, infectious wound on the subcutaneous injection site of MOG. (ii) In the EAE model, mice were dead or had to be euthanized before the start of any treatment. (iii) For mice receiving the intracisternal injection, mice were excluded if they show signs of ataxia, imbalance, paralysis, or death due to the unsuccessful injection. The sample size for different experiments was based on previous publications and the availability of samples and was in accordance with the 3R principle. The *n* for the individual experiment was indicated in the figure legends, and the number of repetitions was also indicated. We defined and removed potential outliers using Graphpad Prism 8 with the built-in ROUT analysis ( $Q = 10\%$ ). Blinding was performed during data collection and analysis. Representative images from immunostaining were obtained from the subjects in randomly chosen areas.

### Experimental animals

Male and female C57BL/6NTac mice (Taconic) were bred at the Comparative Medicine Department at Karolinska University Hospital, Sweden. Animals were maintained in a pathogen-free and climate-controlled environment with regulated 12-h light/dark cycles. All mice used for experiments were adults between 2 and 4 months of age, weighing 20–30 g, and had access to chow and water *ad libitum*.

### Ethics statement

Most animal experiments were performed at Karolinska Institutet and are approved and performed following the Swedish National

Board of Laboratory Animals and the European Community Council Directive (86/609/EEC) and the local ethics committee of Stockholm North under the ethical permits N138/14, followed by 9328-2019. The LPS-challenged mice survival experiment was performed at Fudan University where experimental protocols and animal handling procedures were approved by the Animal Care and Use Committee (ACUC) of Fudan University. For human brain tissue staining, the rapid autopsy regimen of the Netherlands Brain Bank in Amsterdam (coordinator-I Huitinga) was used to acquire the samples with the approval of the Medical Ethical Committee of the Amsterdam UMC.

### Connectivity Map-based drug screening

A public GEO dataset GSE76737 was utilized, which contains the gene expression profile of human microglia using a human gene ST 2.0 Microarray Chip (Affymetrix). The human microglia were polarized to either pro-inflammatory (M1) or immunoregulatory (M2a/M2c/Mtgfb) subtypes using the indicated stimuli: M1 (+LPS/IFN $\gamma$ ), M2a (+IL-4/IL-13), M2c (+IL-4/IL-10/IL-13), and Mtgfb (+TGF $\beta$ ). The differential gene expression pattern from M0->M2a/M2c/Mtgfb and M1->M2a/M2c/Mtgfb was identified using the GEO2R tool. The top 1,000 differential genes were selected; the up-regulated genes and the down-regulated genes were identified. Up-regulated and down-regulated genes from each polarizing pattern were converted to identifiers based on the Affymetrix HG-U133A chip, followed by analysis using *Connectivity Map* (O2 version: broadinstitute.org/cmap). In each pattern, CMAP ranks the compounds using an algorithm based on their correlation to induce the pattern and gives a CMAP score for each compound with “+1” indicating the strongest positive correlation and “-1” being the strongest negative correlation. The GRP files needed for *ConnectivityMap* input were provided in the Dataset EV1.

### Primary cell culture

Primary bone marrow-derived macrophages and primary adult mouse microglial cell cultures were established based on our previous protocol with modifications (Zhang et al, 2014). For mouse, bone marrow-derived macrophages C57BL/6NTac mice were euthanized using CO<sub>2</sub> inhalation and the femurs were dissected. Single-cell suspensions of bone marrow cells were prepared and resuspended in Dulbecco's modified Eagle's medium (DMEM; Sigma-Aldrich, D6046) supplemented with 10% heat-inactivated fetal bovine serum (FBS; Sigma-Aldrich, F7524), 10 ng/ml recombinant mouse M-CSF (R&D Systems, 416-ML), 2 mM L-glutamine (Sigma-Aldrich, G7513), 100 U/ml penicillin, and 100  $\mu$ g/ml streptomycin (Sigma-Aldrich, P4458). The cells were cultured in a T175-cell culture flask with a green lid (Sarstedt, 83.3912.502) and half the cell medium was changed on day 4 and fully changed on day 6, followed by harvest after 7–8 days by prewarmed 0.05% Trypsin-EDTA (Gibco, 25300096) and plated in cell culture plates for indicated experiments. For primary adult microglia, brains from 3-month-old C57BL/6NTac mice were dissected after cardiac perfusion with cold PBS under overdose of pentobarbital sodium anesthesia. The dissected brain was firstly dissociated by physical cutting using a scalpel in a petri dish until no large tissue chunk was visible, followed by enzymatic dissociation with 5 ml enzymatic solution

using papain (Worthington, LS003126; 1:100 diluted in L15 medium). The enzymatic solution containing the brain tissue was then incubated in a 37°C water bath for 15 min, with pipetting in between every 5 min; DNase I (Roche, 10104159001) was added into the solution at a final concentration of 0.2 mg/ml, followed by another incubation for 10 min. The enzymatic solution containing the homogenized brain was transferred to a 50-ml tube, and the enzymatic reaction was terminated by adding 20 ml cold HBSS, followed by passing through a 40  $\mu$ m cell strainer and centrifuging at 300 g, 5 min, 4°C. The cell pellets were then resuspended in 20 ml 38% isotonic Percoll (Sigma-Aldrich, P1644) in HBSS, followed by centrifugation at 800 g (acceleration 4 $\times$ , no brake) for 10 min to remove myelin (floating on top after centrifuge); mixed glial cell pellets were resuspended in DMEM/F12 complete medium containing 10% FBS, 20 ng/ml recombinant mouse M-CSF (R&D Systems, 416-ML), 2 mM L-glutamine (Sigma-Aldrich, G7513), 100 U/ml penicillin, and 100  $\mu$ g/ml streptomycin (Sigma-Aldrich, P4458). Mixed glial cells were cultured and expanded for 10–14 days with medium change twice a week, and when the cells became confluent, they were harvested using prewarmed 0.05% Trypsin-EDTA (as described above). For the separation of microglia from the mixed glial culture, we employed magnetic bead separation using anti-CD11b MicroBeads (MiltenyiBiotec, 130-049-601) following the manufacturer's protocol.

### Cell stimulation and treatment

To induce an inflammatory response in macrophages and microglia, we used 100 ng/ml LPS and 20 ng/ml IFN $\gamma$  to incubate cells for indicated time depending on the experimental purpose; 1  $\mu$ M campothecin (CPT) or topotecan (TPT) were added to the cell culture 30 min before LPS/IFN $\gamma$  stimulation. For flow cytometry analysis, cells were cultured in 24-well plates ( $5 \times 10^5$  per well) for 24 h, and the supernatants were saved for cytokine analysis or nitric oxide assay; for western blotting, cells were cultured in 6-well plates ( $1 \times 10^6$  per well) for 3/6/12 h; for RT-PCR, cells were cultured in 96-well plates ( $5 \times 10^4$  per well) for indicated time points; for immunocytochemistry (fluorescence), cells were cultured in black 96-well plates ( $2 \times 10^4$  per well) for 6 h.

### Cytotoxicity assay

The cytotoxicity of drugs on the cultured cells was measured by the release of LDH (an indicator of cytotoxicity) using a CytoTox 96 Non-Radioactive Cytotoxicity Assay (Promega, G1780) following the provided technical bulletin.

### Reverse transcription-polymerase chain reaction (RT-PCR)

Total RNA of cells or brain tissue (hippocampus and hypothalamus) were automatically isolated using QIAcube (Qiagen, 9001292) with the RNeasy mini kit (Qiagen, 74106) according to the product instructions and underwent 15-min on-column DNase digestion using an RNase-Free DNase Set (Qiagen, 79254). cDNA was prepared with reverse transcriptase using an iScript kit (BioRad Laboratories, 1708891) following the standard protocol provided. Amplifications were conducted using SYBR green (BioRad Laboratories, 1708886) according to the manufacturer's instructions and the

384-well plates were run in a BioRad CFX384 Touch Real-Time PCR Detection System. Primers were designed to work at approximately +60°C and the specificity was assessed by melt curve analysis of each reaction indicating a single peak. The primers used for *Mus musculus* in this study are listed in Appendix Table S1.

### Nitric oxide detection and cytokine analysis

The measurement of nitric oxide (NO) in the supernatants was taken using the modified Griess reagent (Sigma, G4410). Samples (100 µl) were plated in a flat 96-well plates (Corning), mixed with equal volumes of freshly prepared Griess reagent, and incubated for 15 min at room temperature. The plate was read at 540 nm using a microplate reader (LabSystems). The cytokine release to the supernatants was measured using BD™ Cytometric Bead Array (CBA) following the manufacturer's protocol and detected using a BD FACSVerse flow cytometer. The following kits were used to detect indicated cytokines: Mouse IL-6 Flex Set (BD, 558301), Mouse TNF Flex Set (BD, 558299), Mouse MCP-1 Flex Set (BD, 558342), and Mouse IL-10 Flex Set (BD, 558300). The cytokine level in the supernatant was reflected by the median fluorescence intensity (MFI) of PE of the corresponding capture beads.

### LPS challenge

We followed a previous protocol and injected a single dose of systemic lipopolysaccharide (LPS, 5 mg/kg, i.p) which induces severe neuroinflammation (Qin *et al*, 2007). 10 µl of TPT (0.1 mg/kg) or PBS was delivered directly to the CNS before LPS injection via intracisternal injection under isoflurane inhalation. In another experimental setting, we also injected 10 ng LPS to the CNS via intracisternal injection and administered TPT (1 mg/kg, i.p) to evaluate its effect on counteracting LPS-induced neuroinflammation. We also employed a lethal dose LPS challenge (18 mg/kg, i.p) based on a previous study to examine the overall protective effect of TPT on endotoxic shock (Yano *et al*, 2008). TPT (1 mg/kg, i.p) was administered 1 h before a lethal dose of LPS challenge, and mice were kept for a maximum of 96 h.

### Explorative behavioral test

To evaluate the cognitive function following the LPS challenge, we evaluated novel object-evoked curiosity following the methods from previous studies with modifications (Henry *et al*, 2008; Haba *et al*, 2012). Briefly, 24 h post-LPS challenge (5 mg/kg), mice were placed in an observation cage with a novel object (a fluffy teddy bear toy; diameter 5 cm) placed in the center of the cage; the behaviors were videotaped for 5 min. The cumulative number of times the mouse investigated the toy (e.g., touching, sniffing, and trailing) was determined from the video records by a trained observer who was blind to the experiments.

### Induction of experimental autoimmune encephalomyelitis (EAE)

EAE was induced based on previous protocols in our lab with modifications (Berglund *et al*, 2020). In brief, recombinant mouse myelin oligodendrocyte glycoprotein (MOG; amino acids 1–125 from the N terminus) was expressed in *Escherichia coli* (*E. coli*) and purified to

homogeneity by using chelate chromatography following a previous protocol (Liñares *et al*, 2004). Purified MOG was dissolved in 6 M urea followed by dialysis against phosphate-buffered saline (PBS) to obtain a soluble preparation using a Minilys Homogenizer (Bertin Instruments). For EAE induction, mice (20–30 g, 2–4 months, male mice or female mice) were immunized subcutaneously in the dorsal tail base with 35 µg of MOG in PBS emulsified in a 1:1 ratio with complete Freund's adjuvant (Chondrex, 7027) containing 100 µg of Mycobacterium tuberculosis per mouse, under isoflurane (Baxter, 1001936040) inhalation. To facilitate the induction of EAE, 200 ng pertussis toxin (Sigma, P7208) in 200 µl PBS were injected (i.p) before rMOG1-125 immunization and 48 h after immunization. Mice were weighed and fed with wet food daily from day 7 post-immunization, and scored according to the following scheme: 0 = no clinical score, 0.5 = reduced tail tension, 1 = drooping tail (no tonus), 1.5 = drooping tail with clumsy gait, 2 = hindlimb paraparesis, 2.5 = one hindlimb dragging with paraparesis in the other hindlimb, 3 = hindlimb paralysis, 3.5 = hindlimb paralysis with forelimb paraparesis, 4 = tetraplegia or moribund, 5 = death. Mice were euthanized when they showed >25% weight loss or prolonged tetraplegia for more than 3 days without signs of recovery. Dead mice or sacrificed mice were scored 5 on the day of death or sacrifice and scored 4 throughout the following experimental days. The clinical symptoms were scored daily in a blinded manner.

### Intracisternal injection

We followed a previous protocol to perform intracisternal injection (Furlan *et al*, 2003). In brief, mice were anesthetized under isoflurane inhalation, with the head bending forwards to expose the aperture between the occiput and the atlas. A 27G dental needle (Terumo, DN-2721) with the tip (around 3.5 mm) bent at an angle of approx 40° connected with a Hamilton syringe via a polyethylene tube was inserted into the cisterna magna. Up to 10 µl of the solution was slowly injected in approx 10 s.

### Immunofluorescent staining

For immunocytofluorescence, cells were fixed in 100 µl 4% PFA at room temperature for 20 min, washed with PBS (three times 5-min washing), and incubated with blocking buffer (PBS containing 0.1% Triton X-100 and 5% normal goat or donkey serum) for 30 min at +4°C, followed by incubation with the following primary antibodies diluted in antibody dilution buffer (PBS containing 0.1% Triton X-100 and 1% BSA) for overnight at +4°C: rabbit anti-TOP1 (Invitrogen, PA5-82658, 1:200), rabbit anti-Ikaros (Cell Signaling Technology, #14859, 1:200), or rabbit anti-iNOS antibody (Novus Biologicals, NB300-605SS, 1:200). After the rinse, the cells were incubated with goat anti-rabbit 633 (Invitrogen, A21070, 1:500) or Alexa Fluor 488 Phalloidin (Invitrogen, A12379, 1:300) for 30 min at room temperature, followed by co-staining with Hoechst for 5 min (Thermo Scientific, 62249, 1:10,000). For mouse CNS tissue staining, mice were euthanized with an overdose of pentobarbital sodium, followed by perfusion with ice-cold HBSS, and the tissues were fixed in 4% PFA for 48 h followed by dehydration in 20 and 30% sucrose. The tissues were embedded with OCT cryo-mountant (Histolab, 45830) before being put on dry ice and kept at –80°C. Sections (14 µm) were prepared in a cryostat (Leica, CM1850) and kept at –20°C. For human

tissues (5 $\mu$ m), sections were prepared on a microtome, deparaffinized, and rehydrated. Afterward, a gentle antigen retrieval step was performed by putting the sections in a 70°C antigen retrieval solution (Invitrogen, 00-4955-58) for 30 min, followed by PBS washing (for TOP1/Ikaros staining, the sections were then immersed in 20% methanol in PBS for 30 min at room temperature, and washed with PBS for three times). Sections were then blocked with blocking buffer for 1 h at room temperature, followed by primary antibody incubation overnight at 4°C: rabbit anti-Iba1 (Wako Chemicals, 019-19741, 1:400), rabbit anti-CD11b (Abcam, ab128797, 1:400), rabbit anti-TOP1 (Invitrogen, PA5-82658, 1:200), rat anti-F4/80 (Bio-Rad, MCA497GA, 1:200), rabbit anti-Ikaros (Cell Signaling Technology, #14859, 1:200) or mouse anti-HLA-DR (eBioscience, 14-9956-82, 1:750). After rinsing with PBS, the sections were incubated with donkey anti-rabbit, anti-mouse, or anti-rat antibodies labeled with either 488, 594, 633, or 647 (Invitrogen, 1:500) for 1 h at room temperature. For myelin staining, the sections were stained with Fluoromyelin Green (Invitrogen, F34651, 1:300) for 30 min. Sections were co-stained with Hoechst as described above before mounting. Confocal images were acquired with either Leica SP5 or Zeiss LSM880 microscope and analyzed using ImageJ default plugins for co-localization and staining intensity.

### Western blotting and cytokine array

For tissue homogenates, intracardially perfused mice were decapitated and the brains and spinal cords were dissected out and frozen on dry ice. Microglial cells seeded at densities of  $0.5 \times 10^6$  cells/well were stimulated with LPS/IFN $\gamma$  or PBS for indicated hours. Both cells and tissues were homogenized by sonication in RIPA buffer (Sigma-Aldrich, R0278) supplemented with a 1 $\times$  protease and phosphatase inhibitor (Thermo Fisher Scientific, 1861261), and 5 nM phenylmethylsulfonyl fluoride (Thermo-Fisher Scientific, 36978). The homogenates were centrifuged at +4°C for 20 min at 11,000 g. The protein content of the supernatants was determined using a BCA protein assay kit (Thermo Fisher Scientific, 23225) following the manufacturer's protocol. Samples containing equal amounts of proteins were added to 4 $\times$  Laemmli sample buffer (Bio-Rad, 1610747), electrophoresed in 4–20% Mini Protean TGX precast protein gels (Bio-Rad, 4561093), and transferred to a 45 mm nitrocellulose membrane (Bio-Rad, 1620115). After blocking with 5% non-fat dried milk (Applichem, A0830) in TBS-T (20 mM Tris-HCl, pH 7.6, 137 mM NaCl, and 0.1% Tween 20) for 30 min at room temperature, the membrane was incubated overnight at +4°C with TOP1 antibodies (Abcam, ab85038, 1:1,000; Invitrogen PA5-82658, 1:1,000) in blocking solution. The blots were washed for  $3 \times 10$  min with TBS-T and incubated with HRP-linked anti-rabbit secondary antibody (1:30,000, Cell Signalling Technology, 7074S) for 2 h at room temperature. After rinsing in TBS-T for 30 min, the blots were incubated for 5 min with Clarity Western ECL (Bio-Rad, 170-5061), and the chemiluminescence was detected using a Bio-Rad Chemidoc Imaging System. The intensity of the bands was quantified with the Bio-Rad Image Lab software. The data were normalized to  $\beta$ -actin/GAPDH as the loading control. For the cytokine array on brain homogenates, we used the Proteome Profiler Mouse Cytokine Array Kit (R&D Systems, ARY006) following the protocol provided, and developed the membrane in the same manner as we did for Western blot.

### Flow cytometry

Single-cell suspensions were plated into 96-well V-bottom plates and stained at 4°C for 20 min. Dead cells were removed using Live/Dead Fixable Near-IR or Yellow Dead Cell Stain Kit (Invitrogen, L34976 or L34959, 1:500) in each panel. For the analysis of spinal cord myeloid cells, the following antibodies were used as follows: PE anti-mouse Ly-6C (BioLegend, 128008, clone HK1.4, 1:200), PerCP/Cyanine5.5 anti-mouse/human CD11b (BioLegend, 101228, clone M1/70, 1:100), PE/Cyanine7 anti-mouse CD45 (BioLegend, 103114, clone 30-F11, 1:100), and V450 anti-Mouse Ly-6G (BD Biosciences, 560603, clone 1A8, 1:200). For measurement of TNF- $\alpha$  cytokine production in microglia, cells were stimulated with LPS/IFN $\gamma$  as described above and GolgiPlug (BD Biosciences, 555029, 1  $\mu$ l/ml) for 5–6 h, followed by surface staining with APC/Cyanine7 anti-mouse F4/80 (BioLegend, clone BM8, 123118, 1:100). Then, cells were treated with fixation/permeabilization buffer (eBioscience, 00-5123 and 00-5223) for at least 1 h and followed by intracellular staining with PE-Cyanine7 anti-TNF alpha (eBioscience, 25-7423-82, clone TN3-19.12, 1:100). Cells were acquired using a Gallios flow cytometer (Beckman Coulter) and analyzed using Kaluza software (Beckman Coulter). For spleen myeloid panel analysis, we used PE anti-mouse Ly-6C (BioLegend, 128008, clone HK1.4, 1:200), V450 anti-Mouse Ly-6G (BD Biosciences, 560603, clone 1A8, 1:200), PerCP/Cyanine5.5 anti-mouse/human CD11b (BioLegend, 101228, clone M1/70, 1:100), and PE/Cyanine7 anti-mouse F4/80 (BioLegend, 123114, clone BM8, 1:100); for spleen T cell analysis, we used PerCP/Cyanine5 anti-mouse CD3 $\epsilon$  (BioLegend, 100328, clone 145-2C11, 1:100), FITC anti-mouse CD4 (BD Biosciences, 553729, clone GK1.5, 1:100), PE anti-mouse CD8 (eBioscience, 12-0081-81, clone 53-6.7, 1:100), and V450 anti-human/mouse Ki67 (BD Horizon, 561281, clone B56, 1:100). For the cytokine analysis, splenocytes were incubated with stimulated with Ionomycin (Sigma-Aldrich, I0634), PMA (Sigma-Aldrich, P1585) and GolgiPlug (BD Biosciences, 555029) for 5–6 h, and then we first stained PerCP/Cyanine5.5 anti-mouse/human CD11b (BioLegend, 101228, clone M1/70, 1:100) and PE/Dazzle 594 anti-mouse CD4 (BioLegend, 100566, clone RM4-5, 1:100), followed by intracellular staining with PE anti-IL10 (eBioscience, 12-7101-41, clone JES5-16E3, 1:100), PE-Cyanine7 anti-TNF alpha (eBioscience, 25-7423-82, clone TN3-19.12, 1:100), V450 anti-Ki67 (BD Horizon, 561281, clone B56, 1:100), A700 anti-Foxp3 (eBioscience, 56-5773-82, clone FJK-16s, 1:100), FITC anti-GM-CSF (eBioscience, 11-7331-82, clone MP1-22E9, 1:100), and APC anti-IFN gamma (BD Pharmingen, 554413, clone XMG1.2, 1:100). For analysis of Cy5-labeled Glu-HR uptake in different population of immune cells in splenocytes, the following antibodies were used: A488 anti-mouse CD19 (BioLegend, 115521, clone 6D5, 1:100), PE-CF594 anti-Mouse CD3e (Biosciences, 562286, 145-2C11, 1:200), PerCP/Cyanine5.5 anti-mouse/human CD11b (BioLegend, 101228, clone M1/70, 1:100), PE/Cyanine7 anti-mouse CD45 (BioLegend, 103114, clone 30-F11, 1:100), A700 anti-mouse CD11c (BioLegend, 117320, clone N418, 1:100), V450 Rat anti-mouse Ly-6G (Biosciences, 560603, clone 1A8, 1:200). Cells were acquired using a FACSVerse flow cytometer (BD Biosciences) and analyzed using Flowjo 10.7.2.

### Cell sorting

After myelin removal of brain homogenates, the cell suspensions were stained with the following antibodies: PE anti-mouse Ly-6C

(BioLegend, 128008, clone HK1.4, 1:200), PerCP/Cyanine5.5 anti-mouse/human CD11b (BioLegend, 101228, clone M1/70, 1:100), APC anti-mouse F4/80 (BioLegend, 123116, clone BM8, 1:100), PE/Cyanine7 anti-mouse CD45 (BioLegend, 103114, clone 30-F11, 1:100), and Live/Dead Fixable Yellow Dead Cell Stain Kit (Invitrogen, L34959, 1.500). The CD11b<sup>+</sup>CD45<sup>+</sup>Ly6C<sup>-</sup>F4/80<sup>int</sup> cells were sorted and collected using a SONY SH800 Cell Sorter. For magnetic-activated cell sorting of splenocytes, the spleens were mashed, followed by red blood cells removal using ACK lysis buffer (Gibco, A1049201). The cell suspension was first incubated with anti-CD11b MicroBeads (MiltenyiBiotec, 130-049-601), and the on-column CD11b<sup>+</sup> cells were collected as the myeloid cells. The uncollected non-myeloid (CD11b<sup>-</sup>) cells were processed with the Pan T Cell Isolation Kit (MiltenyiBiotec, 130-095-130) following the manufacturer's protocol, and the untouched T cells were collected, whereas the on-column cells were flushed and collected as the B cells.

### Next-generation RNA sequencing

Microglia were sorted directly into TRIzol reagent (Invitrogen, 15596-018) and kept at  $-80^{\circ}\text{C}$  before sending to BGI Genomics (Hong Kong, China) for RNA extraction and sequencing. Total RNA was extracted using a phenol-chloroform extraction following the provided protocol of TRIzol. Total RNA was qualified and quantified using a NanoDrop and Agilent 2100 bioanalyzer (Thermo Fisher Scientific, MA, USA). Limited RNA of more than 200 pg was amplified with oligo-dT and dNTPs, incubated at  $72^{\circ}\text{C}$ , immediately put back on the ice, and reverse transcribed to cDNA based on polyA tail. The template was switched to the 5' end of the RNA and the full-length cDNA was generated by PCR. Agilent 2100 bioanalyzer instrument (Thermo Fisher Scientific, MA, USA) was used to determine the average molecule length of the PCR product. Purified cDNA from previous steps was fragmented into small pieces with a fragment buffer by PCR, and the product was purified and selected by the AgencourtAMPure XP-Medium kit (Thermo Fisher Scientific, USA). cDNA was quantified by Agilent Technologies 2100 bioanalyzer. The double-stranded PCR product undergoing the QC step was heat-denatured and circularized by the splint oligo sequence. The single-strand circle DNA (ssCir DNA) was formatted as the final library. The final library was quantitated in two ways to ensure the high quality of the sequencing data: Determined the average molecule length using the Agilent 2100 bioanalyzer instrument, the quantified library used real-time quantitative PCR (qPCR). The final library was amplified with phi29 (Thermo Fisher Scientific, MA, USA) to make a DNA nanoball (DNB) which had more than 300 copies of one molecular, DNBS were loaded into the patterned nanoarray and pair-end 100 bases reads were generated on BGISEQ500 platform (BGI-Shenzhen, China).

### RNA-seq data processing

RNA-seq read quality was assessed using FastQC (<https://www.bioinformatics.babraham.ac.uk/projects/fastqc/>). Reads were trimmed using Trimmomatic (Bolger *et al*, 2014) and mapped to mouse transcripts sequence (GRCm38), counted, normalized, and quantified (TPM, transcripts per million) by Salmon (Patro *et al*, 2017). The raw counting table was imported and summarized by tximport (Soneson *et al*, 2015), followed by differential gene

expression analysis with EdgeR (Robinson *et al*, 2010). Significantly deregulated genes were identified by a false discovery rate lower than 0.05. Gene set enrichment analysis of gene ontology (GO) and Kyoto Encyclopedia of Genes and Genomes (KEGG) pathway was performed with ClusterProfiler (Yu *et al*, 2012). Transcription factor prediction was performed using BART (Wang *et al*, 2018) and HOMER (Heinz *et al*, 2010) with the differentially expressed genes identified by EdgeR. All the scripts used for bioinformatics analyses are available onGithub: [https://github.com/KeyiG/LPS\\_TPT\\_RNA-seq.git](https://github.com/KeyiG/LPS_TPT_RNA-seq.git). The RNA-seq data are available in the ArrayExpress repository, under accession numbers: E-MTAB-10679.

### Human brain tissue processing

Human brain tissues were acquired from MS patients diagnosed according to the McDonald criteria and age-matched controls without neurological conditions (Polman *et al*, 2005). Controls were identified and selected from a larger cohort based on their pathological and clinical profile. Some controls were excluded if they had medical records of neurological disorders, cancer, or other inflammatory diseases of the CNS. We followed the rapid autopsy regime of the Netherlands Brain Bank in Amsterdam (coordinator Dr. I. Huitinga) to obtain donor tissues. Participants or next of kin were informed and consented to the brain autopsy procedure and the use of their tissue for research purposes. Tissues were fixed in 4% paraformaldehyde, processed and paraffin-embedded. Tissues of MS brains were selected and classified based on the size and type of lesion for quantitative analyses. Identification of the lesions was acquired by immunohistochemistry for myelin proteolipid protein PLP to detect myelin loss and HLA-DR to detect myeloid cell activation (van der Valk & De Groot, 2000).

### Gene Expression Omnibus data mining

Several datasets from Gene Expression Omnibus (GEO) were revisited and mined for examining TOP1 expression. GSE97930 and GSE73721 analyzed by the Brain Myeloid Landscape 2 (<http://research-pub.gene.com/BrainMyeloidLandscape>) were used for comparing TOP1 expression in different brain cell types in healthy humans (Srinivasan *et al*, 2020). Datasets GSE85333 (from stimulated primary human macrophages), GSE108000 (from brain white matter of MS patients and healthy donors), and GSE18920 (from spinal cords of sporadic ALS patients or healthy donors) were analyzed with GEO2R, and the relative mRNA expression of TOP1 was plotted. CHIP-seq data from GSE93602 was used to analyze the occupancy of Ikaros at the transcriptional start sites (TSS) of genes of interest.

### DNA origami preparation and characterization

Single-stranded scaffold DNA p7560 production: in a shaker at  $37^{\circ}\text{C}$ , we cultured 250 ml *E. coli* strain JM109 in  $2\times$  YT medium (Sigma-Aldrich) containing 5 mM  $\text{MgCl}_2$  (Sigma-Aldrich) to  $\text{OD}_{600}$  0.5. The bacteriophage M13mp18 derivative was added to the bacteria culture at an infection multiplicity of 1 for 4 h shaking amplification. We spun down the bacteria at 4,000 g for 30 min and collected the supernatant. After adding 10 g PEG8000 (VWR) and 7.5 g NaCl (VWR) to the collected supernatant, we incubated it with ice for

30 min and centrifuged it at 10,000 *g* for 30 min to pellet the phage. The phage pellet was then re-suspended in a 10 ml Tris buffer (10 mM, pH 8.5, VWR), followed by the addition of 10 ml NaOH (0.2 M, VWR)—SDS (1%, VWR) buffer. After this, we denatured the phage protein coat by adding 7.5 ml of KOAc (3 M, pH 5.5, VWR) for a 10-min incubation on ice. Denatured phage proteins were precipitated by centrifuging at 16,500 *g* for 30 min. The supernatant containing scaffold DNA p7560 was kept and purified by the method of ethanol precipitation. We kept the final scaffold DNA p7560 in Tris buffer (10 mM, pH 8.5, VWR), and measured its concentration using a UV-Vis A260 Nano-Drop (Thermo Scientific).

**Topotecan-DNA nanostructure folding and purification:** We ordered 100- $\mu$ M staple oligonucleotides (IDT) in 96-well plates. All the staple oligonucleotides were then mixed to be the staple DNA pool (400 nM for each oligonucleotide). Materials used for a 100- $\mu$ l structure folding were as follows: 10  $\mu$ l of single-stranded scaffold DNA p7560 (200 nM), 25  $\mu$ l of the staple DNA pool, 5  $\mu$ l of topotecan (TPT; 100  $\mu$ M), 10  $\mu$ l of 10 $\times$  PBS and 50  $\mu$ l of Milli-Q water. We folded the DNA nanostructure into a hexagonal rod shape (HR) via an annealing program as follows: a rapid heat denaturation (80°C for 5 min) followed by cooling from 80°C to 60°C over 20 min, then from 60°C to 24°C over 14 h. We purified and concentrated the folded structures by using an Amicon 100K filter tube (Millipore), which included six times washing with 1 $\times$  PBS at 5,000 *g* for 2 min. The concentrations of the HR DNA origami nanostructures were then measured at UV-Vis A260 on Nano-Drop (Thermo Scientific).

**TPT loading capacity of the HR DNA origami nanostructure:** During the purification process of TPT-HR via Amicon 100K filter tube (Millipore), all filtrates were collected. The unloaded free TPT in the filtrates was quantified via a fluorescence-based assay on a multimode microplate reader (Varioskan<sup>TM</sup> LUX). The maximum excitation and emission wavelength for TPT measurement are 390 and 538 nm, respectively. The drug loading efficiency (%) was calculated by the following equation: Loading efficiency (%) =  $(D_{\text{total}} - D_{\text{free}})/D_{\text{total}} \times 100$ .  $D_{\text{total}}$  is the amount of TPT added for loading;  $D_{\text{free}}$  is the amount of TPT in the filtrate.

**In vitro TPT release profile measurement:** We used the dialysis units with a molecular weight cutoff of 12 kDa (Merck) to carry out the drug release experiments. At 37°C protected from light, the structure samples were added to the dialysis unit, which was then dialyzed in 1,000 ml 1 $\times$  PBS (pH = 7.4) at a stirring speed of 200 rpm. At certain time intervals, 10  $\mu$ l of samples were taken out from the dialysis unit for measuring the non-released TPT by a multimode microplate reader (Varioskan<sup>TM</sup> LUX). To test the response of drug release to DNase, at certain time points, Benzonase (0.5 U/ $\mu$ l, Invitrogen) and MgCl<sub>2</sub> (2 mM) were added to both the dialysis units and the drug release media.

**Glucan coating of the TPT-HR nanostructure:** We pre-designed 60 single-stranded polyA<sub>50</sub> protrusions, which were sites for the binding of glucan, around the HR structure. To coat the purified HR structures, glucan (Sigma Aldrich) dissolved in DMSO was added to the TPT-HR nanostructure with the molar ratio of glucan/polyA<sub>50</sub> protrusion at 2/1. The sample was then kept under 4°C overnight for coating. We washed away DMSO and free samples by using an Amicon 100K filter tube (Millipore). The glucan-coated TPT-HR nanostructure is named MyloGami throughout the study.

## Agarose gel electrophoresis

Agarose (Sigma-Aldrich) gels (2%) were cast in 0.5 $\times$  TBE buffer (VWR) supplemented with 10 mM MgCl<sub>2</sub> and 0.5 mg/ml ethidium bromide (Sigma Aldrich). Within the ice water bath, electrophoresis was carried out in a 0.5 $\times$  TBE buffer supplemented with 10 mM MgCl<sub>2</sub> at 90 volts for 90 min. We imaged gels by using a GE LAS 4000 imager.

## Transmission electron microscopy

A 5  $\mu$ l (5 nM) structured DNA origami, sample was spotted on a glow-discharged, carbon-coated, formvar resin grid (Electron Microscopy Sciences) for 20 s. We then blotted the sample with a filter paper, and next stained the grid with 2% (w/v) aqueous uranyl formate solution (Electron Microscopy Sciences). After drying, we imaged the sample under an FEI Morgagni 268 transmission electron microscope at 80 kV.

## Real-time HR to cell interaction measurement

We pre-coated the MutilDish 2  $\times$  2 (LigandTracer) with 0.1% (w/v) Poly-L-lysine solution (Sigma-Aldrich) under 37°C for 30 min, after which we gently washed the MutilDish 2  $\times$  2 three times with 1 $\times$  PBS (pH = 7.4). 20 million B cells, T cells, or myeloid cells collected from mice splenocytes were seeded into one sector of the coated MutilDish 2  $\times$  2 for a 2-h attachment in a cell culture incubator. We then took out the MutilDish 2  $\times$  2 and added Cy5-labeled DNA origami nanostructures to the cells. At room temperature, real-time interactions of Cy5-labeled DNA origami nanostructures to cells were monitored with LigandTracer Green (Ligand Tracer).

## Statistical analysis

Statistical analyses were performed with GraphPad Prism 8, and a  $P < 0.05$  was considered significant. In general, data were presented as group means  $\pm$  SEM. The Student's unpaired two-tailed *t*-test was used to compare the difference when two groups were compared, and one-way ANOVA with Dunnett's or Tukey's Multiple Comparison test for comparison for more than two groups. For EAE score-based analyses (average, cumulative, and max EAE score), the Kruskal-Wallis test with Dunn's multiple-comparisons test was used when more than 2 groups were compared, and the Mann-Whitney *U* test was used to compare between two groups. The area under the curve (AUC) of the EAE clinical course approaches continuous variable with normal distribution despite the EAE score being ordinal and was therefore compared using either one-way ANOVA with Dunnett's or Tukey's Multiple Comparison test (more than two groups) or Student's unpaired two-tailed *t*-test (between two groups). We specified the detailed statistical analyses for each graph in the corresponding figure legends.

## Data availability

All data associated with this study are present in the paper. RNA-seq results are available in the ArrayExpress repository (E-MTAB-10679)

with the following link: <https://www.ebi.ac.uk/arrayexpress/experiments/E-MTAB-10679/>

**Expanded View** for this article is available online.

## Acknowledgements

We thank Tojo James for converting the gene symbols to the Affymetrix HG-U133A probe identifiers. We thank ElianePiket for introducing the techniques for intracisternal injection. We appreciate the practical help and suggestions from former PhD members in our unit, Karl Carlström and Marie N'diaye, and EAE statistical suggestion from Prof. Maja Jagodic. We thank Sebastian Lewandowski for providing insights about ALS and related scientific discussions. We appreciate Feng Yang's advice on the artwork design. We are grateful to the staff at our animal facility (AKM) for animal caretaking, and to the people at our Neuroimmunology Unit, especially Mohsen Khademi, Gunn Jönsson, and Hamid Dadkhodai. We also thank the fundings that supported our study: the Swedish Research Council/Vetenskapsrådet 2021-01926 (RAH), the StratNeuro funding for Collaborative Neuroscience Projects at Karolinska Institutet (RAH and BH), the Swedish Neurofonden Foundation F2020-0017 (KZ), the China Scholarship Council 201700260280 (KZ) and 201700260271 (KG), the National Natural Science Foundation of China 82074538 (JW), and the UPPMAX SNIC project 2020/16-223 and 2020/15-292 (CK).

## Author contributions

**Keying Zhu:** Conceptualization; Data curation; Formal analysis; Funding acquisition; Validation; Investigation; Visualization; Methodology; Writing—original draft; Project administration; Writing—review & editing. **Yang Wang:** Data curation; Formal analysis; Validation; Investigation; Visualization; Methodology; Writing—original draft; Writing—review & editing. **Heela Sarlus:** Data curation; Formal analysis; Validation; Investigation; Visualization; Methodology; Writing—original draft; Writing—review & editing. **Keyi Geng:** Resources; Data curation; Software; Formal analysis; Visualization; Methodology; Writing—original draft; Writing—review & editing. **Erik Nutma:** Data curation; Validation; Investigation; Methodology; Writing—original draft; Writing—review & editing. **Jingxian Sun:** Data curation; Validation; Investigation; Methodology. **Shin-Yu Kung:** Data curation; Validation; Investigation; Methodology. **Cindy Bay:** Data curation; Validation; Investigation; Methodology. **Jinming Han:** Investigation; Methodology. **Jin-Hong Min:** Investigation. **Irene Benito-Cuesta:** Validation. **Harald Lund:** Supervision; Writing—review & editing. **Sandra Amor:** Resources; Supervision; Writing—original draft; Writing—review & editing. **Jun Wang:** Resources; Supervision; Funding acquisition; Writing—review & editing. **Xing-Mei Zhang:** Formal analysis; Supervision; Methodology; Writing—review & editing. **Claudia Kutter:** Resources; Data curation; Software; Formal analysis; Supervision; Writing—review & editing. **André Ortlieb Guerreiro-Cacais:** Formal analysis; Supervision; Methodology; Writing—review & editing. **Björn Högberg:** Resources; Software; Supervision; Funding acquisition; Investigation; Methodology; Writing—original draft; Writing—review & editing. **Robert A Harris:** Conceptualization; Resources; Supervision; Funding acquisition; Writing—original draft; Project administration; Writing—review & editing.

In addition to the CRediT author contributions listed above, the contributions in detail are:

KZ conceived, designed, and planned this project; he also performed the *Connectivity Map* analysis as well as most of the experiments, with input from RAH, XMZ, AO, and HL; YW, KZ, RAH, and BH designed MyloGami and TopoGami, and YW produced these nanomaterials and tested their basic properties under the supervision of BH. For RNA-seq, KZ sorted the cells and prepared the samples for sequencing; KG performed the RNA-seq data analyses, plotted the figures for

publication, and uploaded the codes under the supervision of CK. HS performed the Western blotting experiments and helped with flow cytometry and sorting. EN performed the histostaining on human brain sections under the supervision of SA. The survival experiment following the LPS challenge was performed by JS under the supervision of JW; JS also tested TPT in a cuprizone-induced demyelinating model and JW also provided help with Connectivity Map. Master students S-YK and CB performed *in vitro* experiments under the practical supervision of KZ; S-YK also helped with dissections, animal behavioral tests, and analyses, as well as scoring the EAE mice. JH induced MOG-EAE and scored the EAE mice. XMZ provided technical support on *in vitro* cell culture and analyses of flow cytometry data. AOG-C produced MOG, performed experiments of tail blood analysis, and provided technical support for flow cytometry and *in vivo* experiments. J-HM helped with primary cell and cell line cultures. I-BC helped with cytometric beads assays. KZ, YW, HS, and KG wrote the manuscript with suggestions from all authors, especially RAH for revising and editing the whole manuscript, and BH, AOG-C, CK, HL for editing the corresponding part of the manuscript.

## Disclosure and competing interests statement

The authors declare that they have no conflict of interest.

## References

- Aouadi M, Tencerova M, Vangala P, Yawe JC, Nicoloso SM, Amano SU, Cohen JL, Czech MP (2013) Gene silencing in adipose tissue macrophages regulates whole-body metabolism in obese mice. *Proc Natl Acad Sci USA* 110: 8278–8283
- Aouadi M, Tesz GJ, Nicoloso SM, Wang M, Chouinard M, Soto E, Ostroff GR, Czech MP (2009) Orally delivered siRNA targeting macrophage Map4k4 suppresses systemic inflammation. *Nature* 458: 1180–1184
- Benson E, Mohammed A, Gardell J, Masich S, Czeizler E, Orponen P, Högberg B (2015) DNA rendering of polyhedral meshes at the nanoscale. *Nature* 523: 441–444
- Berglund R, Guerreiro-Cacais AO, Adzemovic MZ, Zeitelhofer M, Lund H, Ewing E, Ruhmann S, Nutma E, Parsa R, Thessen-Hedreul M *et al* (2020) Microglial autophagy-associated phagocytosis is essential for recovery from neuroinflammation. *Sci Immunol* 5: abb5077
- Bernier L-P, York EM, Kamyabi A, Choi HB, Weilingner NL, MacVicar BA (2020) Microglial metabolic flexibility supports immune surveillance of the brain parenchyma. *Nat Commun* 11: 1559
- Bocian W, Kawecki R, Bednarek E, Sitkowski J, Williamson MP, Hansen PE, Kozerski L (2008) Binding of topotecan to a nicked DNA oligomer in solution. *Chemistry* 14: 2788–2794
- Bolger AM, Lohse M, Usadel B (2014) Trimmomatic: a flexible trimmer for Illumina sequence data. *Bioinformatics* 30: 2114–2120
- Brehm BR, Bock C, Wesselborg S, Pfeiffer S, Schüler S, Schulze-Osthoff K (2001) Prevention of human smooth muscle cell proliferation without induction of apoptosis by the topoisomerase I inhibitor topotecan. *Biochem Pharmacol* 61: 119–127
- Cassinelli V, Oberleitner B, Sobotta J, Nickels P, Grossi G, Kempter S, Frischmuth T, Liedl T, Manetto A (2015) One-step formation of “Chain-Armor”-stabilized DNA nanostructures. *Angew Chem Int Ed Engl* 54: 7795–7798
- Chernov L, Deyell RJ, Anantha M, Dos Santos N, Gilabert-Oriol R, Bally MB (2017) Optimization of liposomal topotecan for use in treating neuroblastoma. *Cancer Med* 6: 1240–1254
- Cho S-J, Huh J-E, Song J, Rhee D-K, Pyo S (2008) Ikaros negatively regulates inducible nitric oxide synthase expression in macrophages: involvement of Ikaros phosphorylation by casein kinase 2. *Cell Mol Life Sci* 65: 3290–3303

- Constantinescu CS, Farooqi N, O'Brien K, Gran B (2011) Experimental autoimmune encephalomyelitis (EAE) as a model for multiple sclerosis (MS). *Br J Pharmacol* 164: 1079–1106
- Douglas SM, Bachelet I, Church GM (2012) A logic-gated nanorobot for targeted transport of molecular payloads. *Science* 335: 831–834
- Fernández-Arjona MDM, Grondona JM, Granados-Durán P, Fernández-Llebrez P, López-Ávalos MD (2017) Microglia morphological categorization in a rat model of neuroinflammation by hierarchical cluster and principal components analysis. *Front Cell Neurosci* 11: 235
- Foo EC, Russell M, Lily O, Ford HL (2020) Mitoxantrone in relapsing-remitting and rapidly progressive multiple sclerosis: ten-year clinical outcomes post-treatment with mitoxantrone. *Mult Scler Relat Disord* 44: 102330
- Francis OL, Payne JL, Su R-J, Payne KJ (2011) Regulator of myeloid differentiation and function: the secret life of Ikaros. *World J Biol Chem* 2: 119–125
- Furlan R, Pluchino S, Marconi PC, Martino G (2003) Cytokine gene delivery into the central nervous system using intrathecally injected nonreplicative viral vectors. *Methods Mol Biol* 215: 279–289
- Girstun A, Ishikawa T, Staron K (2019) Effects of SRSF1 on subnuclear localization of topoisomerase I. *J Cell Biochem* 120: 11794–11808
- Haba R, Shintani N, Onaka Y, Wang H, Takenaga R, Hayata A, Baba A, Hashimoto H (2012) Lipopolysaccharide affects exploratory behaviors toward novel objects by impairing cognition and/or motivation in mice: possible role of activation of the central amygdala. *Behav Brain Res* 228: 423–431
- Hartung H-P, Gonsette R, König N, Kwiecinski H, Guseo A, Morrissey SP, Krapf H, Zwingers T & Mitoxantrone in Multiple Sclerosis Study Group (MIMS) (2002) Mitoxantrone in progressive multiple sclerosis: a placebo-controlled, double-blind, randomised, multicentre trial. *Lancet* 360: 2018–2025
- Healy LM, Perron G, Won SY, Michell-Robinson MA, Rezk A, Ludwin SK, Moore CS, Hall JA, Bar-Or A, Antel JP (2016) MerTK Is a functional regulator of myelin phagocytosis by human myeloid cells. *J Immunol* 196: 3375–3384
- Healy LM, Perron G, Won SY, Michell-Robinson MA, Rezk A, Ludwin SK, Moore CS, Hall JA, Bar-Or A, Antel JP (2016) Gene Expression Omnibus GSE76737 (<https://www.ncbi.nlm.nih.gov/geo/query/acc.cgi?acc=GSE76737>) [DATASET]
- Heinz S, Benner C, Spann N, Bertolino E, Lin YC, Laslo P, Cheng JX, Murre C, Singh H, Glass CK (2010) Simple combinations of lineage-determining transcription factors prime cis-regulatory elements required for macrophage and B cell identities. *Mol Cell* 38: 576–589
- Henry CJ, Huang Y, Wynne A, Hanke M, Himler J, Bailey MT, Sheridan JF, Godbout JP (2008) Minocycline attenuates lipopolysaccharide (LPS)-induced neuroinflammation, sickness behavior, and anhedonia. *J Neuroinflammation* 5: 15
- Ho JSY, Mok B-Y, Campisi L, Jordan T, Yildiz S, Parameswaran S, Wayman JA, Gaudreault NN, Meekins DA, Indran SV et al (2021) TOP1 inhibition therapy protects against SARS-CoV-2-induced lethal inflammation. *Cell* 184: 2618–2632.e17
- Husain A, Begum NA, Taniguchi T, Taniguchi H, Kobayashi M, Honjo T (2016) Chromatin remodeller SMARCA4 recruits topoisomerase 1 and suppresses transcription-associated genomic instability. *Nat Commun* 7: 10549
- International Multiple Sclerosis Genetics Consortium (2019) Multiple sclerosis genomic map implicates peripheral immune cells and microglia in susceptibility. *Science* 365: eaav7188
- Jordão MJC, Sankowski R, Brendecke SM, Sagar M, Locatelli G, Tai Y-H, Tay TL, Schramm E, Armbruster S, Hagemeyer N et al (2019) Single-cell profiling identifies myeloid cell subsets with distinct fates during neuroinflammation. *Science* 363: eaat7554
- Joshi H, Sengupta A, Gawwala K, Hazra P (2014) Unraveling the mode of binding of the anticancer drug topotecan with dsDNA. *RSC Adv* 4: 1015–1024
- Kiviahio JK, Linko V, Ora A, Tiainen T, Järvihaavisto E, Mikkilä J, Tenhu H, Nonappa N, Kostianen MA (2016) Cationic polymers for DNA origami coating—examining their binding efficiency and tuning the enzymatic reaction rates. *Nanoscale* 8: 11674–11680
- Lamb J, Crawford ED, Peck D, Modell JW, Blat IC, Wrobel MJ, Lerner J, Brunet J-P, Subramanian A, Ross KN et al (2006) The Connectivity Map: using gene-expression signatures to connect small molecules, genes, and disease. *Science* 313: 1929–1935
- Lauro C, Limatola C (2020) Metabolic reprogramming of microglia in the regulation of the innate inflammatory response. *Front Immunol* 11: 493
- Lepka K, Volbracht K, Bill E, Schneider R, Rios N, Hildebrandt T, Ingwersen J, Prozorovski T, Lillig CH, van Horssen J et al (2017) Iron-sulfur glutaredoxin 2 protects oligodendrocytes against damage induced by nitric oxide release from activated microglia. *Glia* 65: 1521–1534
- Li F, Li H, Zhang S (2011) Ikaros expression in tongue sole macrophages: a marker for lipopolysaccharide- and lipoteichoic acid-induced inflammatory responses. *Mol Biol Rep* 38: 2273–2279
- Liñares D, Echevarria I, Mañá P (2004) Single-step purification and refolding of recombinant mouse and human myelin oligodendrocyte glycoprotein and induction of EAE in mice. *Protein Expr Purif* 34: 249–256
- Ma W, Zhan Y, Zhang Y, Mao C, Xie X, Lin Y (2021) The biological applications of DNA nanomaterials: current challenges and future directions. *Signal Transduct Target Ther* 6: 351
- Marazzi I, Greenbaum BD, Low DHP, Guccione E (2018) Chromatin dependencies in cancer and inflammation. *Nat Rev Mol Cell Biol* 19: 245–261
- McCauley ME, O'Rourke JG, Yáñez A, Markman JL, Ho R, Wang X, Chen S, Lall D, Jin M, Muhammad AKMG et al (2020) C9orf72 in myeloid cells suppresses STING-induced inflammation. *Nature* 585: 96–101
- Mishra MK, Yong VW (2016) Myeloid cells — targets of medication in multiple sclerosis. *Nat Rev Neurol* 12: 539–551
- Mougiakakos D, Bach C, Böttcher M, Beier F, Röhner L, Stoll A, Rehli M, Gebhard C, Lischer C, Eberhardt M et al (2021) The IKZF1-IRF4/IRF5 axis controls polarization of myeloma-associated macrophages. *Cancer Immunol Res* 9: 265–278
- Némati F, Daniel C, Arvelo F, Legrier M-E, Froget B, Livartowski A, Assayag F, Bourgeois Y, Poupon M-F, Decaudin D (2010) Clinical relevance of human cancer xenografts as a tool for preclinical assessment: example of *in-vivo* evaluation of topotecan-based chemotherapy in a panel of human small-cell lung cancer xenografts. *Anticancer Drugs* 21: 25–32
- Norris G, Derecki N, Kipnis J (2014) Microglial sholl analysis. *Protoc Exch*. <https://doi.org/10.1038/protex.2014.029>
- O'Rourke JG, Bogdanik L, Yáñez A, Lall D, Wolf AJ, Muhammad AKMG, Ho R, Carmona S, Vit JP, Zarrow J et al (2016) C9orf72 is required for proper macrophage and microglial function in mice. *Science* 351: 1324–1329
- Oh K-S, Gottschalk RA, Lounsbury NW, Sun J, Dorrington MG, Baek S, Sun G, Wang ZE, Krauss KS, Milner JD et al (2018) Dual roles for Ikaros in regulation of macrophage chromatin state and inflammatory gene expression. *J Immunol* 201: 757–771
- Oh K-S, Gottschalk RA, Lounsbury NW, Sun J, Dorrington MG, Baek S, Sun G, Wang Z, Krauss KS, Milner JD et al (2018) Gene Expression Omnibus GSE93602 (<https://www.ncbi.nlm.nih.gov/geo/query/acc.cgi?acc=GSE93602>) [DATASET]
- Patro R, Duggal G, Love MI, Irizarry RA, Kingsford C (2017) Salmon provides fast and bias-aware quantification of transcript expression. *Nat Methods* 14: 417–419
- Polman CH, Reingold SC, Edan G, Filippi M, Hartung H-P, Kappos L, Lublin FD, Metz LM, McFarland HF, O'Connor PW et al (2005) Diagnostic criteria

- for multiple sclerosis: 2005 revisions to the “McDonald Criteria”. *Ann Neurol* 58: 840–846
- Pommier Y (2006) Topoisomerase I inhibitors: camptothecins and beyond. *Nat Rev Cancer* 6: 789–802
- Ponnuswamy N, Bastings MMC, Nathwani B, Ryu JH, Chou LYT, Vinther M, Li WA, Anastassacos FM, Mooney DJ, Shih WM (2017) Oligolysine-based coating protects DNA nanostructures from low-salt denaturation and nuclease degradation. *Nat Commun* 8: 15654
- Qin L, Wu X, Block ML, Liu Y, Breese GR, Hong J-S, Knapp DJ, Crews FT (2007) Systemic LPS causes chronic neuroinflammation and progressive neurodegeneration. *Glia* 55: 453–462
- Rialdi A, Campisi L, Zhao N, Lagda AC, Pietzsch C, Ho JSY, Martinez-Gil L, Fenouil R, Chen X, Edwards M *et al* (2016) Topoisomerase 1 inhibition suppresses inflammatory genes and protects from death by inflammation. *Science* 352: aad7993
- Rinne M, Mätlik K, Ahonen T, Vedovi F, Zappia G, Moreira VM, Yli-Kauhaluoma J, Leino S, Salminen O, Kalso E *et al* (2020) Mitoxantrone, pixantrone and mitoxantrone (2-hydroxyethyl)piperazine are toll-like receptor 4 antagonists, inhibit NF- $\kappa$ B activation, and decrease TNF- $\alpha$  secretion in primary microglia. *Eur J Pharm Sci* 154: 105493
- Robinson MD, McCarthy DJ, Smyth GK (2010) edgeR: a Bioconductor package for differential expression analysis of digital gene expression data. *Bioinformatics* 26: 139–140
- Rothemund PWK (2006) Folding DNA to create nanoscale shapes and patterns. *Nature* 440: 297–302
- Saijo K, Collier JG, Li AC, Katzenellenbogen JA, Glass CK (2011) An ADIOL-ER $\beta$ -CtBP transrepression pathway negatively regulates microglia-mediated inflammation. *Cell* 145: 584–595
- Sakurai K, Uezu K, Numata M, Hasegawa T, Li C, Kaneko K, Shinkai S (2005)  $\beta$ -1,3-glucan polysaccharides as novel one-dimensional hosts for DNA/RNA, conjugated polymers and nanoparticles. *ChemInform* 36: 4383–4398
- Sanada Y, Matsuzaki T, Mochizuki S, Okobira T, Uezu K, Sakurai K (2012)  $\beta$ -1,3-D-glucan schizophyllan/poly(dA) triple-helical complex in dilute solution. *J Phys Chem B* 116: 87–94
- Sharma Y, Ahmad A, Yavvari PS, Kumar Muwal S, Bajaj A, Khan F (2019) Targeted SHP-1 silencing modulates the macrophage phenotype, leading to metabolic improvement in dietary obese mice. *Mol Ther Nucleic Acids* 16: 626–636
- Shekhar S, Vatsa N, Kumar V, Singh BK, Jamal I, Sharma A, Jana NR (2016) Topoisomerase 1 inhibitor topotecan delays the disease progression in a mouse model of Huntington’s disease. *Hum Mol Genet* 26: 420–429
- Smale ST, Natoli G (2014) Transcriptional control of inflammatory responses. *Cold Spring Harb Perspect Biol* 6: a016261
- Soneson C, Love MI, Robinson MD (2015) Differential analyses for RNA-seq: transcript-level estimates improve gene-level inferences. *F1000Res* 4: 1521
- Song C, Pan X, Ge Z, Gowda C, Ding Y, Li H, Li Z, Yochum G, Muschen M, Li Q *et al* (2016) Epigenetic regulation of gene expression by Ikaros, HDAC1 and casein kinase II in leukemia. *Leukemia* 30: 1436–1440
- Srinivasan K, Friedman BA, Etxeberria A, Huntley MA, van der Brug MP, Foreman O, Paw JS, Modrusan Z, Beach TG, Serrano GE *et al* (2020) Alzheimer’s patient microglia exhibit enhanced aging and unique transcriptional activation. *Cell Rep* 31: 107843
- Staker BL, Hjerrild K, Feese MD, Behnke CA, Burgin Jr AB, Stewart L (2002) The mechanism of topoisomerase I poisoning by a camptothecin analog. *Proc Natl Acad Sci USA* 99: 15387–15392
- Sung M-H, Li N, Lao Q, Gottschalk RA, Hager GL, Fraser IDC (2014) Switching of the relative dominance between feedback mechanisms in lipopolysaccharide-induced NF- $\kappa$ B signaling. *Sci Signal* 7: ra6
- van der Valk P, De Groot CJ (2000) Staging of multiple sclerosis (MS) lesions: pathology of the time frame of MS. *Neuropathol Appl Neurobiol* 26: 2–10
- Wang Y, Benson E, Fördős F, Loloico M, Baars I, Fang T, Teixeira AI, Högberg B (2021) DNA origami penetration in cell spheroid tissue models is enhanced by wireframe design. *Adv Mater* 33: 2008457
- Wang Z, Civelek M, Miller CL, Sheffield NC, Guertin MJ, Zang C (2018) BART: a transcription factor prediction tool with query gene sets or epigenomic profiles. *Bioinformatics* 34: 2867–2869
- Xu J, Liu D, Yin Q, Guo L (2016) Tetrandrine suppresses  $\beta$ -glucan-induced macrophage activation via inhibiting NF- $\kappa$ B, ERK and STAT3 signaling pathways. *Mol Med Rep* 13: 5177–5184
- Yamasaki R, Lu H, Butovsky O, Ohno N, Rietsch AM, Cialic R, Wu PM, Doykan CE, Lin J, Cotleur AC *et al* (2014) Differential roles of microglia and monocytes in the inflamed central nervous system. *J Exp Med* 211: 1533–1549
- Yang N, Yue R, Ma J, Li W, Zhao Z, Li H, Shen Y, Hu Z, Lv C, Xu X *et al* (2019) Nitidine chloride exerts anti-inflammatory action by targeting Topoisomerase I and enhancing IL-10 production. *Pharmacol Res* 148: 104368
- Yano K, Okada Y, Beldi G, Shih S-C, Bodyak N, Okada H, Kang PM, Luscinskas W, Robson SC, Carmeliet P *et al* (2008) Elevated levels of placental growth factor represent an adaptive host response in sepsis. *J Exp Med* 205: 2623–2631
- Yu G, Wang L-G, Han Y, He Q-Y (2012) clusterProfiler: an R package for comparing biological themes among gene clusters. *OMICS* 16: 284–287
- Zaksauskaite R, Thomas RC, van Eeden F, El-Khamisy SF (2021) Tdp1 protects from topoisomerase 1-mediated chromosomal breaks in adult zebrafish but is dispensable during larval development. *Sci Adv* 7: eabc4165
- Zeng X, Zhu S, Lu W, Huang J, Liu Z, Zhou Y, Hou Y, Huang Y, Guo H, Fang J *et al* (2020) Target identification among known drugs by deep learning from heterogeneous networks. *SSRN Electr J*. <https://doi.org/10.2139/ssrn.3385690>
- Zhang Q, Lin S, Shi S, Zhang T, Ma Q, Tian T, Zhou T, Cai X, Lin Y (2018) Anti-inflammatory and antioxidative effects of tetrahedral DNA nanostructures via the modulation of macrophage responses. *ACS Appl Mater Interfaces* 10: 3421–3430
- Zhang X-M, Lund H, Mia S, Parsa R, Harris RA (2014) Adoptive transfer of cytokine-induced immunomodulatory adult microglia attenuates experimental autoimmune encephalomyelitis in DBA/1 mice. *Glia* 62: 804–817
- Zhao D, Cui W, Liu M, Li J, Sun Y, Shi S, Lin S, Lin Y (2020) Tetrahedral framework nucleic acid promotes the treatment of bisphosphonate-related osteonecrosis of the jaws by promoting angiogenesis and M2 polarization. *ACS Appl Mater Interfaces* 12: 44508–44522



**License:** This is an open access article under the terms of the Creative Commons Attribution-NonCommercial-NoDerivs License, which permits use and distribution in any medium, provided the original work is properly cited, the use is non-commercial and no modifications or adaptations are made.